

pubs.acs.org/JPCC Article

High-Pressure Structural and Thermodynamic Properties of Cerium Orthosilicates (CeSiO₄)

- 3 Published as part of The Journal of Physical Chemistry virtual special issue "Early-Career and Emerging
- 4 Researchers in Physical Chemistry Volume 2".
- 5 Andrew Strzelecki, Xiaodong Zhao, Jason Baker, Paul Estevenon, Thomas Barral, Adel Mesbah,
- 6 Dmitry Popov, Stella Chariton, Vitali Prakapenka, Sohan Ahmed, Choong-Shik Yoo, Nicolas Dacheux,
- 7 Hongwu Xu, and Xiaofeng Guo*



Cite This: https://doi.org/10.1021/acs.jpcc.2c06657



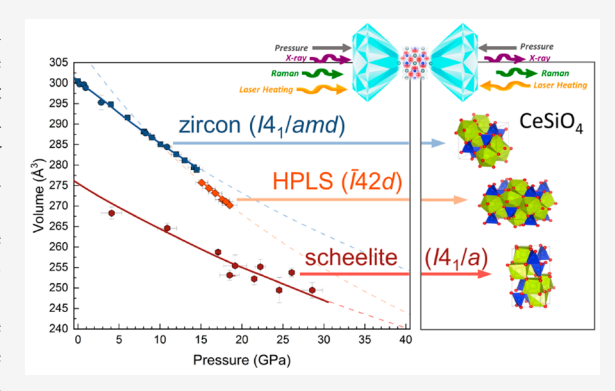
ACCESS

III Metrics & More

Article Recommendations

Supporting Information

8 **ABSTRACT:** Pressure-induced phase transitions from the zircon 9 structure-type $(I4_1/amd)$ to the scheelite structure type $(I4_1/a)$ are 10 known for many ternary oxides systems (ABO₄). In this work, we present 11 the first high-pressure study on synthetic stetindite (CeSiO₄) by a 12 combination of in situ high-pressure synchrotron powder X-ray 13 diffraction up to 36 GPa, implemented with and without dual sided 14 laser heating, and in situ high-pressure Raman spectroscopy up to 43 15 GPa. Two phase transitions were identified: zircon to a high-pressure 16 low-symmetry (HPLS) phase at 15 GPa and then to a scheelite at 18 17 GPa. The latter from HPLS scheelite phase was found irreversible; i.e., 18 scheelite is fully quenchable at ambient conditions, as in other zircon-type 19 phases. The bulk moduli (K_0) of stetindite, HPLS, and high-pressure 20 scheelite phases were determined respectively as 171(5), 105(4), and



21 221(40) GPa by fitting to a second-order Birch-Murnaghan equation of state The pressure derivatives of vibrational modes and 22 Grüneisen parameters of the zircon-structured polymorph is similar to those of other orthosilicate minerals. Due to the larger ionic 23 radii of Ce^{4+} , with respect to Zr^{4+} , stetindite was found to possess a softer bulk modulus and undergo the phase transitions at a lower 24 pressure than zircon $(ZrSiO_4)_{ij}$ such observations are consistent with what were found with coffinite $(USiO_4)$.

1. INTRODUCTION

25 Pressure-induced phase transitions from the zircon structure-26 type (space group: I41/amd) to the scheelite structure-type 27 (space group: $I4_1/a$) are known for many different ternary 28 oxides (ABO₄). ^{1,2} These ABO₄ systems include orthosilicates 29 (ZrSiO₄, HfSiO₄ and USiO₄), ³⁻⁹ heavy rare earth element 30 (HREE) orthophosphates (HREEPO₄), 10-14 and rare earth 31 element (REE) orthovanadates (REEVO₄). 15-21 The most 32 studied of these phases is the eponymous orthosilicate mineral, 33 zircon (ZrSiO₄), which undergoes a phase transition between 34 20 and 30 GPa, depending on the composition of natural 35 samples used (i.e., concentrations of Hf, U, or REE) and 36 degree of metamictization. 3-6,22-28 This high-pressure phase 37 of ZrSiO₄ has been identified in natural systems such as the 38 ejecta associated with meteorite impacts and was given a 39 mineral name, reidite (scheelite structure type; space group: 40 $I4_1/a$). The pressure-induced phase transition from zircon to 41 reidite results in an approximately 10% increase in the overall 42 density, with the [001] channels of zircon being completely 43 eliminated in reidite (Figure 1). 2,30 More recently, an 44 intermediate phase between zircon and reidite has been

reported to occur between 20 and 25 GPa. ^{22,31} This new high- ⁴⁵ pressure polymorph has been referred to a high-pressure low- ⁴⁶ symmetry (HPLS) phase (space group: $\overline{I4}_2d$), resulting from ⁴⁷ slight rotation and twisting of the SiO₄ and MO₈ polyhedra in ⁴⁸ the zircon structure (Figure 1). ^{22,31}

Studying high-pressure transitions of zircon-type materials 50 also has important thermophysical implications for their 51 applications. Materials possessing the zircon structure tend to 52 have low chemical reactivity, low solubility, and good 53 resistance to radiation damage, which make them ideal 54 candidates for ceramic based waste hosts for the permanent 55 immobilization of actinides from nuclear wastes. In 56 particular the use of zircon has been proposed for the disposal 57 of plutonium (Pu) associated with the defense program since 58

Received: September 18, 2022 Revised: January 3, 2023



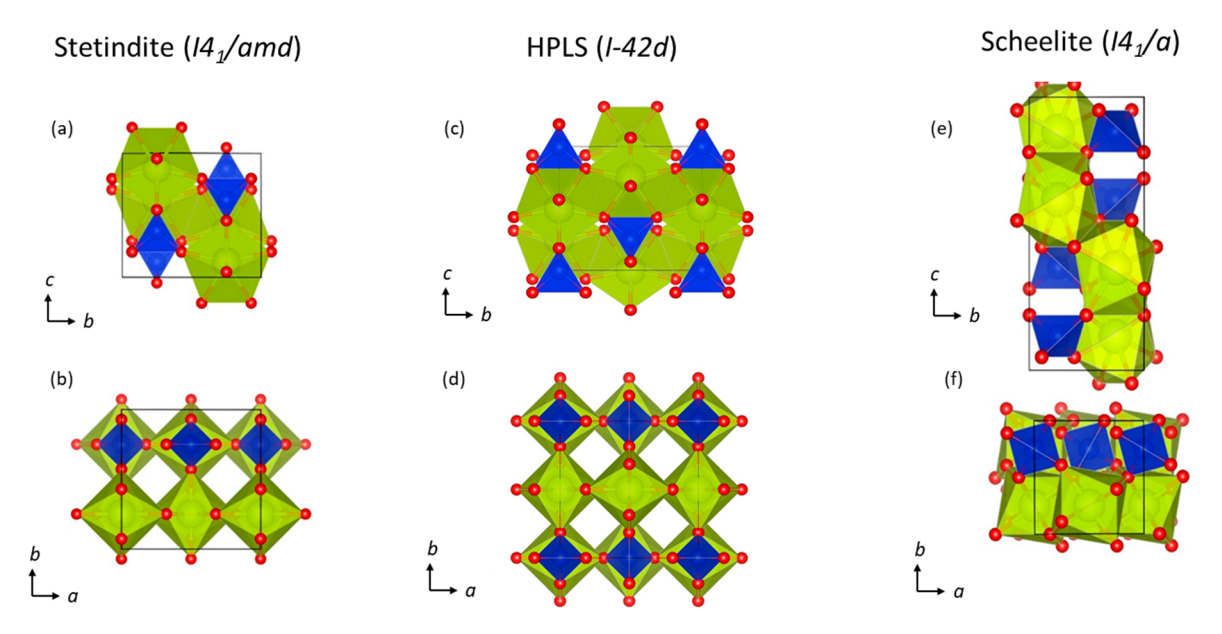


Figure 1. Crystal structures of the low-pressure stetindite phase $(I4_1/amd)$, the intermediate-pressure HPLS phase $(\overline{I4}_2d)$, and the high-pressure scheelite phase $(I4_1/a)$. (a, c, e) Projected along the a-axis. (b, d, f) Projected along the c-axis..

59 the 1990s.³⁸ Studying the thermochemical and thermophysical 60 properties of ceramic waste hosts is paramount in order to 61 confidently model and predict their long-term behavior during 62 storage. 38-46 However, synthesizing the PuSiO₄ phase is 63 difficult. 47,48 Thus, examining Pu-surrogate silicate is a rational 64 approach to understand material behaviors and properties of 65 $PuSiO_4$. Because the ionic radius of Ce^{4+} (0.97 Å) is similar to 66 that of Pu⁴⁺ (0.96 Å) in an 8-fold coordination environment, ⁴⁹ 67 equivalent to the MO₈ snub-disphenoid of the zircon structure-68 type, Ce is an effective surrogate for approximating the solid 69 state behavior of Pu. 50-53 Ce can be incorporated in the zircon 70 structure and form pure phase CeSiO₄, with its natural 71 occurrence, stetindite, discovered in Norway in 2009.⁵⁴ 72 However, no high-pressure (high-P) studies have been 73 reported for stetindite, partly because stetindite is also very 74 difficult to synthesize. 55,36 The advent of synthetic stetindite 75 has allowed for several recent studies to investigate some of its 76 thermochemical 57,58 and thermophysical properties. 59 In this 77 work, we continue to study the thermophysical properties of 78 synthetic stetindite by examining its structural behavior under 79 high pressures as determined by a combination of in situ high-80 pressure synchrotron powder X-ray diffraction up to 36 GPa, 81 implemented with and without dual sided laser heating, and in 82 situ high-pressure Raman spectroscopy up to 43 GPa.

2. EXPERIMENTAL METHODS

2.1. Sample Synthesis. Two batches of synthetic stetindite (CeSiO₄) were prepared in this study. Each batch was synthesized hydrothermally, in accordance to the protocol described by Estevenon et al., in which a Ce³⁺-silicate solid precursor (A-Ce₂Si₂O₇) was used. A-Ce₂Si₂O₇ was synthesized by solid state route, in which a stoichiometric mixture of CeO₂ (Sigma-Aldrich; particle size < 5 μ m) and SiO₂ (Sigma-90 Aldrich, 10–20 nm) were mechanically milled (30 Hz, 1 h) in a Retsch MM 200 vibration mill mixer using a tungsten carbide milling vessel. The resulting mixture was pelletized by uniaxial pressing under 5 MPa at room temperature and then heated at 1350 °C under a reducing atmosphere (Ar–4% H₂) to produce A-Ce₂Si₂O₇. 200 mg of the Ce³⁺-silicate solid

precursor was then placed in contact with 4 mL of a 0.75 M 96 HNO₃ solution (prepared by dilution of ACS grade 70% 97 HNO₃, Sigma-Aldrich). In the synthesis of the first batch of 98 CeSiO₄ (later used in in situ high-pressure synchrotron XRD 99 with Ne as a pressure transmitting medium, PTM), the acidity 100 of the solution was adjusted to a pH of 7.0 \pm 0.1 with a freshly 101 prepared NaOH solution (from ACS grade NaOH pellets, 102 Sigma-Aldrich). In the second batch of CeSiO₄ (later used in 103 the in situ high-pressure laser-heated synchrotron XRD 104 experiment in which KCl was used as the PTM), the acidity 105 of the solution was adjusted to a pH 6.5 \pm 0.1, again with a 106 freshly prepared NaOH solution (from ACS grade NaOH 107 pellets, Sigma-Aldrich). Moreover, in the second batch, an 108 excess of 8 mol % Si was added to the mixture (8.8 mg of 109 Na₂SiO₃·5H₂O) to avoid the CeO₂ formation. In both batches, 110 the mixtures were then hydrothermally treated for 7 days at 111 150 °C under air atmosphere using a Parr autoclave. The final 112 products were separated from the supernatant solution by 113 centrifugation, washed twice with deionized water and once 114 with ethanol, and then finally dried overnight at 60 °C. The 115 final products of both synthetic routes lead to single phased 116 CeSiO₄ of high crystallinity. 56,57,59

2.2. In Situ High-Pressure Synchrotron XRD. The 118 pressure generated in this study was done through a Princeton- 119 type symmetric DAC. The sample was loaded in a laser-drilled 120 hole (150 μ m diameter) at the center of a pre-indented (45 121 μ m thickness) steel gasket, which was encapsulated between 122 two diamonds (culet size: 300 μ m). The gasket was drilled 123 using the High-Pressure Collaborative Access Team (HPCAT) 124 laser drilling system at the Advanced Photon Source (APS), 125 Argonne National Laboratory (ANL).⁶⁰ Two ruby spheres 126 were placed into the sample cavity as the pressure calibrant. 127 Pressure was obtained by using the standard ruby pressure 128 scale based on a pressure-induced shift of the R₁ fluorescence 129 line of ruby, measured by an online fluorescence spectrometer 130 system, which employs a 532 nm laser. 61,62 Ne gas was used as 131 the PTM and was loaded using the GeoSoilEnviroCARS 132 (GSECARS) gas loading system at APS, ANL to an initial 133 pressure of 4.0 \pm 0.2 GPa.⁶³ The loaded DAC was then 134

135 transferred to the HPCAT beamline 16-BM-D at APS, ANL, 136 where in situ high-pressure XRD measurements were 137 conducted. The X-ray wavelength used was 0.4133 Å (30 138 keV), with a beam size of $5 \times 5 \mu \text{m}^2$. Two-dimensional (2D) 139 diffraction images were collected using a Mar 345 detector, and 140 the geometric parameters were calibrated using a CeO₂ 141 standard. The sample to detector distance was fixed at 299.5 142 mm. All collected two-dimensional images were calibrated, 143 masked, and integrated through the use of Dioptas. 64 The 144 obtained XRD patterns of stetindite and high-pressure phases 145 were analyzed through Rietveld method using the General 146 Structure Analysis System software version II (GSAS-II). 65 147 The background was modeled by the Chebyshev function. The 148 structure reported in Strzelecki et al.⁵⁹ for stetindite at room 149 temperature served as the starting structural model for the 150 refinements of phases under low pressures, the structure 151 reported by Stangarone et al.²² for HPLS zircon served as the 152 starting structural model for the refinements of the 153 intermediate-pressure phase, and the structure reported for 154 high-pressure phase of coffinite (USiO₄) by Zhang et al.⁷ 155 served as the starting model for the refinements for scheelite 156 phase.

2.3. In Situ High-Pressure Laser-Heated Synchrotron 158 **XRD.** The sample and a small piece of Pt powder were placed 159 between two KCl plates. Because KCl is hydroscopic, which 160 can alter the hydrostatic conditions of the experiment, 66 it was 161 dried at 723 K for 24 h prior to being loaded (and was stored 162 in a 373 K drying oven when not in use). KCl was used as the 163 PTM, thermal insulator, and internal pressure marker, and Pt 164 as a laser coupler and a secondary pressure maker. Such a 165 "sandwich" layered mixture was loaded into an electric 166 discharge machine (EDM) drilled hole (150 μ m diameter) 167 at the center of a preiindented (35 μ m thickness) Re gasket. The loaded DAC was then transferred to the GSECARS 169 beamline 13-ID-D at APS, ANL, where in situ high-pressure 170 and high-temperature XRD measurements were conducted. The pressure generated in this study was done through the same Princeton-type symmetric DAC (culet size: 300 μ m) 173 used in the high-pressure synchrotron XRD experiment 174 described above. High temperatures were generated by using 175 the on-site double-sided laser heating system. 67,68 The laser 176 beam was aligned coaxially with the X-ray beam to measure 177 diffraction patterns on the heating spot. The typical beam 178 diameters for the laser heating spots were 10-20 μ m. The 179 temperatures generated during the laser heating was 180 determined spectroradiometerically using the gray-body approximation. The X-rays had a wavelength of 0.3344 Å 182 (37 keV), with a beam size of \sim 2.5 \times 2.5 μ m. The beam 183 geometric parameters were calibrated using LaB₆. The distance 184 from sample to detector was fixed at 236.7 mm. The two-185 dimensional (2D) images were collected utilizing a Pilatus 186 CdTe area detector. All collected two-dimensional images were 187 calibrated, masked, and integrated through the use of 188 Dioptas. 64 The Rietveld refinement on the obtained XRD 189 data were the same as the description in Section 2.2. Based on 190 the pressure-volume equation of state (EOS) of KCl-B1 191 (space group: $Fm\overline{3}m$) and KCl-B2 (space group: $Pm\overline{3}m$) 192 reported by Dewaele et al.,⁷⁰ and the pressure-volume EOS 193 for Pt (space group: $Fm\overline{3}m$) reported by Zha et al., ⁷¹ the 194 pressure in the cell was reported by taking the average of the 195 two derived pressures with the error as two standard deviations 196 of the mean.

2.4. In Situ High-Pressure Raman Spectroscopy. 197 Raman spectroscopic measurements were performed using a 198 Horiba LabRAM HR Evolution Raman spectrometer/micro- 199 scope system of the Radiogeochemistry Team at Los Alamos 200 National Laboratory (LANL). 72,73 A 532 nm laser was utilized 201 for the spectroscopic measurements, and an Olympus 20× 202 long-working-distance objective lens was used to visualize the 203 sample and focus the laser into the sample chamber. All spectra 204 were collected in the 100-1400 cm⁻¹ range. The maximum 205 laser output is 100 mW but is greatly attenuated before 206 interacting with the sample. The system is equipped with an 207 1800 gr/mm which yields an effective resolution of 0.33 cm⁻¹. 208 The collected spectra were corrected by subtracting the 209 background and were fitted using a Lorentz-type function. For 210 the in situ high-pressure Raman spectroscopic measurements, a 211 Princeton-style symmetric DAC with Type IIb, ultralow 212 fluorescence 300 μ m culet diamonds (Almax) were used to 213 generate high pressure. The sample was loaded in a drilled hole 214 (125 μ m diameter) at the center of a pre-indented (50 μ m 215 thickness) stainless-steel gasket. Two ruby microspheres were 216 placed into the sample cavity as the pressure calibrant. The 217 PTM used was a 4:1 methanol: ethanol mixture. The sample 218 was compressed from room pressure up to 43.3 ± 2.2 GPa, and 219 Raman spectra were collected on both compression and 220 decompression. In addition, the sample recovered after the in 221 situ high P-T synchrotron XRD was also analyzed by Raman 222 spectroscopy after being removed from the DAC. This was 223 done by placing the recovered gasket onto a glass slide.

3. RESULTS

3.1. In Situ High-Pressure Synchrotron XRD. Powder 225 X-ray diffraction patterns at various pressures during 226 compression and decompression are shown in Supporting 227 Information Figure S1. Figure S2 shows representative fitted 228 patterns of CeSiO₄ at 4.0 \pm 0.2, 15.1 \pm 0.8, and 36.0 \pm 1.8 229 GPa. During compression at room temperature, stetindite was 230 stable up to 14.5 ± 0.7 GPa, at which point it began to 231 transform to HPLS (Figure S1). The HPLS phase persisted 232 from 15.1 \pm 0.8 to 18.5 \pm 0.9 GPa, above which it began to 233 convert to scheelite. The phase transition to scheelite was 234 complete at 29.9 \pm 1.5 GPa, in which no more reflections 235 attributed to the HPLS structure could be found (Figure S1). 236 The scheelite structure was found to persist when the sample 237 was decompressed to the lowest pressure possibly achieved, 238 14.7 \pm 0.7 GPa. Refinements for stetindite from 4.0 \pm 0.2 to 239 14.5 \pm 0.7 GPa yielded $R_{\rm wp}$ values between 0.895% and 240 0.997% (Table S1). Refinements performed on the HPLS 241 phase from 15.1 \pm 0.8 to 18.5 \pm 0.9 GPa yielded $R_{\rm wp}$ values 242 between 0.927% and 1.12% (Table S2). Refinements of high- 243 pressure phases from 33.0 \pm 1.7 to 36.0 \pm 1.8 GPa during 244 compression and all phases during decompression yielded R_{wp} 245 values between 1.25% and 1.41% (Table S3). Rietveld analyses 246 of the XRD patterns at high pressures were difficult because of 247 the broad diffraction peaks caused by the deviatoric stresses 248 (Figure S1).⁷⁴

In addition to the silicate phases, there was a presence of a 250 low diffuse peak around 8° (2θ), possibly attributing to the 251 (200) reflection of ice-(VI),⁷⁵ shown in Figure S2a, which was 252 observed during the compression from 4.0 ± 0.2 to 18.5 ± 0.9 253 GPa. While the presence of ice-(VI) is not consistent with the 254 phase diagram of water,^{76,77} it is the only likely phase which 255 would attribute a diffraction peak at the two-theta range it is 256 observed. Other phases that were considered, but did fit the 257

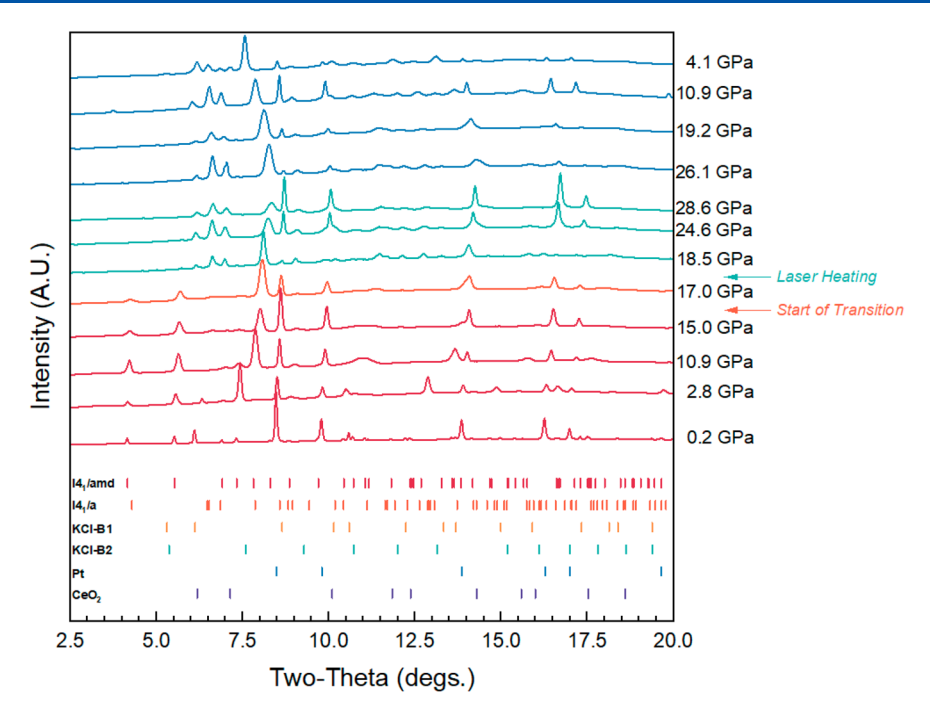


Figure 2. Selected powder X-ray diffraction patterns of $CeSiO_4$ at high pressures. From bottom to top, the patterns were collected during the increase of pressure up to 28.6 GPa. The cell was laser heated at a pressure of 17.0 GPa. The ticks above the x-axis indicate the positions of allowed diffraction maxima.

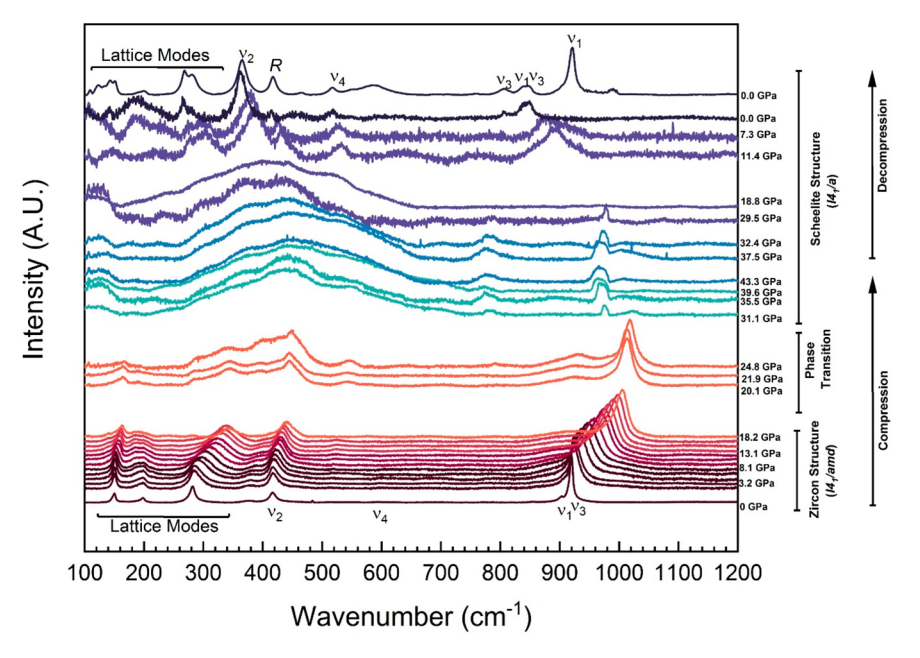


Figure 3. Raman spectra of CeSiO₄ at ambient conditions and in situ high pressures up to 43.3 GPa and then decompressed back to ambient conditions. The spectrum presented at the top of the figure was collected on the sample recovered after being compressed and laser heated at beamline 13-ID-D (APS).

258 measured patterns, were CeO_2 , SiO_2 (α -quartz and coesite), 259 Al_2O_3 , Fe, Ne, as well as ice-(VII). The presence of this extra 260 reflection was not related to the scheelite transition because its 261 occurrence was below transitions of any known zircon-262 structured orthosilicate at ambient temperature, $^{4,6-9}$ while 263 also well within the hydrostatic limit of Ne, ruling out the 264 possibility of an early phase transition due to a steep pressure 265 gradient. Previously, our work has shown that stetindite can 266 retain significant amounts of water (\sim 0.5 mol) as both 267 adsorbed surface water and confined water in the [001]

channels of the zircon structure. 57,59 Thus, it is possible that 268 water crystallizes to ice-(VI) upon compression, 78 which has 269 been widely seen in other minerals and materials, such as more 270 porous zeolites. 79 Because the (200) reflections would 271 correspond to a 4 -spacing of 2 -988(7) Å, it is possible that 272 such ice-(VI) crystallized from the confined water within the 273 [001] channel. So, the existence of ice-(VI) is also possible by 274 that within the [001] channel the 4 -20 experiences a lowered 275 pressure due to capillary pressure effect. The other possibility 276 is that the water—ice transition is still taking place within the 2

278 channel and that really limits the possibility of forming the 279 disordered ice (VII), ⁸⁰ as confined ice will have different 280 thermodynamic equilibrium than that of bulk ice. However, 281 the extra reflection was excluded from the refinements by 282 means of the exclude function in GSAS-II⁶⁵ and consequently 283 was not considered during the whole pattern refinements.

3.2. In Situ High-Pressure Laser-Heated Synchrotron 285 **XRD.** Powder X-ray diffraction patterns from high P-T XRD 286 are shown in Figure 2, with a representative fitting shown in 287 Figure S3. With KCl as the PTM, stetindite was stable up to 288 15.0 \pm 0.9 GPa (Figure 2). This was evident by the appearance 289 of peaks located at 6.654° corresponding to the (112) 290 diffraction plane of the scheelite-structured phase (Figure 291 S4). The sample was further compressed to 17.0 \pm 1.6 GPa 292 (after scheelite transition) and was then subjected to double-293 sided laser heating (Figure 2). Laser heating provided energy 294 to overcome the kinetic hindrance of the zircon-scheelite 295 transformation and relax any accumulated stresses. This is 296 clearly observed by the sharpness in the diffraction peaks (Figure 2), in contrast to those shown in Figure S2. Note that 298 laser heating was not done to map out the P-V-T EOS. The 299 maximum temperature achieved by the present laser heating 300 setup was estimated to be higher than 3000 K. The exact 301 temperature was not able to be determined as a large flash of 302 the laser saturated the detector. Upon laser quenching, well-303 crystallized scheelite with minor amounts of CeO₂ were found. 304 CeO₂ may be resulted from thermal decomposition of CeSiO₄, 305 which is not thermodynamically favorable with respect to its 306 binary oxides under the standard condition.⁵⁷ The cell was 307 then compressed to maximum pressure of 28.6 ± 1.3 GPa, 308 where no further phase transformations were observed (i.e., 309 monazite or fergusonite).81 During decompression, pressure 310 was lowered to 4.1 \pm 1.3 GPa, and the scheelite structure 311 persisted (Figure 2). The resulting Rietveld refinements on the 312 collected patterns yielded $R_{\rm wp}$ values between 1.80% and 7.91% 313 (Tables S4 and S5).

3.3. In Situ High-Pressure Raman Spectroscopy. 315 Collected Raman spectra of CeSiO₄ during the compression 316 from ambient to 43.3 ± 2.2 GPa and decompressed back to 317 ambient are displayed in Figure 3. At room temperature, 318 stetindite was stable up to 18.1 ± 0.9 GPa, in agreement with 319 to the results obtained from XRD. The phase transition to 320 scheelite was completed above 24.8 \pm 1.2 GPa, above of which 321 no more vibration could be attributed to the zircon structure. 322 The scheelite phase was also fully quenchable upon 323 decompression to ambient conditions. Peaks above 31.1 ± 324 1.6 GPa became very broad, with all but two of the vibrational 325 modes being easily distinguished. Upon decompression, the 326 broadness of vibrational modes diminished, indicating that the 327 broadness of them was likely due to the deviatoric stress as the 328 result of the 4:1 methanol: ethanol PTM reaching its 329 hydrostatic limit⁷⁴ and only partially due to amorphization.⁹ Theoretically, the I4₁/amd space group has 17 Raman-active vibrational modes belonging to the \bar{D}_{4h} point group. $^{82-84}$ 332 Among these 17 modes, nine (Γ_{int} = $2A_{1g}$ + $2B_{1g}$ + B_{2g} + $2E_{\sigma}$ 82,84 can be assigned to the internal vibrations (or normal 334 modes) of the SiO₄ tetrahedron, and the remaining eight ($\Gamma_{\rm ext}$ $_{335} = 2B_{1g} + 3E_{g})^{82,84}$ assigned to the external vibrations (lattice modes). The vibrational modes labeled as ν_{1} , ν_{2} , ν_{3} , and 337 ν_4 correspond to the internal vibrations, where ν_1 (A_{1g}) and ν_3 338 (B_{1g}) correspond to the symmetric and antisymmetric 339 stretching motions, respectively, and ν_2 (A_{1g}) and ν_4 (B_{1g})

340 correspond to the symmetric and antisymmetric bending

modes, respectively.⁸⁶ The motion of the external modes can 341 be further be classified into rotational (E_g) and translational 342 $(B_g + E_g)$ modes. 82,86 At ambient conditions, the three external 343 modes appear at 282, 197, and 150 cm⁻¹. Using the 344 assignments of isostructural compounds reported in Syme et 345 al. for ThSiO₄ and ZrSiO₄, 87 as well as the assignments 346 presented in Mihailova et al. 31 and Stangarone et al. for 347 $ZriSO_4$, 22 the vibrational bands can be described by 282 cm⁻¹ 348 (E_g), 197 cm⁻¹ (E_g), and 150 cm⁻¹ (B_{1g}). 9,22,31 To differentiate 349 between the two external modes, which have identical 350 Mulliken symbols, we adopted the notation of Stangarone et 351 al., 22 so the vibrational band found at 197 cm⁻¹ is E_g (1) and 352 that found at 282 cm $^{-1}$ is E_g (2). The B_g and E_g (2) external 353 vibrational modes are translational external modes whereas the 354 E_g (1) external vibrational mode is a rotational external 355 mode. 22,31 Due to the interaction of the SiO₄ tetrahedra with 356 the MO₈ dodecahedra in the unit cell, the SiO₄ tetrahedra 357 cannot be considered a strictly independent unit. 87 As a result 358 of these interactions, there has yet to be a reporting of a 359 spectrum with all 17 of the Raman-active modes for zircon 360 structure-type materials. 83 The peak vibrational positions for 361 stetindite under ambient pressure are displayed in Table 1 362 tl

Table 1. Location of the Internal Vibration Modes of SiO₄ Tetrahedron of Stetindite in cm⁻¹ and Comparison with Those of Some Other Zircon Structure-Type Materials under Ambient Pressures^{55,56,57,8283,85,87,88},

	$ u_1(\mathrm{A}_{1\mathrm{g}}) $	$\nu_2(A_{1g})$	$\nu_3(\mathrm{B}_{2\mathrm{g}})$	$\nu_4(B_{2g})$	Ref
CeSiO ₄	902	417	920	594	This Study
CeSiO ₄	903	431	919	592	Estevenon et al. ⁵⁵
CeSiO ₄	902	431	919	592	Estevenon et al. ⁵⁶
CeSiO ₄	902	416	918	593	Strzelecki et al. ⁵⁹
$ZrSiO_4$	974	439	1008	608	Dawson et al. ⁸²
$HfSiO_4$	984	448	1018	620	Hoskins et al. ⁸⁵
$ThSiO_4$	894	439	920	593	Syme et al. ⁸⁷
$ThSiO_4$	887	438	914	592	Clavier et al. ⁸³
$USiO_4$	904	428	930	N.O.	Geisler et al. ⁸⁸
$USiO_4$	906	424	919	591	Clavier et al. ⁸³
USiO ₄	903	424	918	592	Strzelecki et al. ⁵⁹

alongside other zircon structure-type orthosili- 363 cates. \$5,56,59,8283,85,87,88 The peak position and standard error 364 from each deconvolution are listed in Table S6. The $\overline{I4}_2d$ space 365 group, which the HPLS structure belongs to, has 30 theoretical 366 active Raman vibrational modes ($\Gamma = 3A_1 + 5B_1 + 4B_2 + 9E_g$), 367 based on the D_{2d} point group. The authors recommend the 368 work by Mihailova et al. for a more in depth discussion on the 369 mode analysis of this space group. 31 The $I4_1/a$ space group has 370 18 theoreticaly active Raman vibrational modes ($\Gamma = 3A_g + 5B_g$ 371 + $5E_g$), based upon the C_{4h}^6 point group. $^{89-91}$ Of these 18 372 active modes, nine ($\Gamma_{int} = 2A_g + 3B_g + 2E_g$) can be assigned to 373 the internal vibrations of the SiO_4 tetrahedron, while the 374 remaining nine $(\Gamma_{ext} = A_g + 2B_g + 3E_g)$ can be assigned to the 375 external vibrations within the unit cell. The vibrational 376 modes labeled ν_1 , ν_2 , ν_3 , and ν_4 correspond to the internal 377 vibrations. The symmetric and antisymmetric stretching 378 motions are represented by ν_1 (A_g) and ν_3 (B_g + E_g), 379 respectively, and the symmetric and antisymmetric bending 380 modes correspond to ν_2 (A_g + B_g) and ν_4 (B_g + E_g), 381 respectively. The motion of the external modes can be further 382 be classified into rotational $(A_g + B_g)$ and translational $(2B_g + 383)$ 2E_σ) modes.⁸⁹⁹⁰ The peak position and standard error from 384

385 each deconvolution are listed in Table S7. As with zircon 386 structure-type materials, not all of the vibrational modes are 387 present in the scheelite phase due to lattice interaction. Here 388 we used the peak assignments of Smirnov et al., Gucsik et al., 389 Stangarone et al., Knittle and Williams, Gucsik et al., Manoun 390 et al., Bauer et al., and Kaur and Sinha in order to assign the 391 peaks present in the scheelite-structured phase. 5-7,9,22, 392 The Raman spectra collected during decompression below 393 11.4 GPa, along with the recovered CeSiO₄ from the laser 394 heating experiment resemble that of scheelite (CaWO₄), 395 stolzite (PbWO₄), powellite (CaMoO₄), wulfenite 396 (PbMoO₄), and other tungstate and molybdate minerals and 397 materials. 89,90,94-96

4. DISCUSSION

4.1. Pressure-Volume Equations of State. Figure 4 399 shows the pressure dependence of the unit cell volumes of the

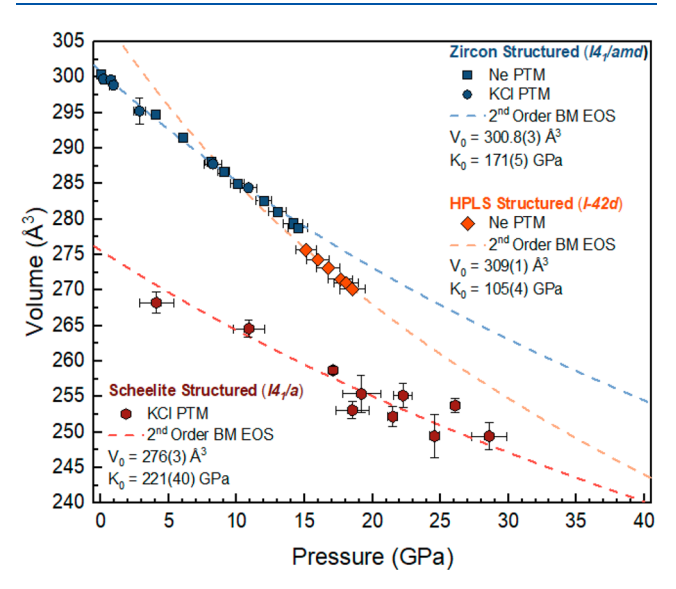


Figure 4. Unit cell volume of CeSiO₄ as a function of pressure. Blue symbols represent the low-pressure zircon-type (I4₁/amd) phase; orange symbols represent the intermediate-pressure HPLS-type $(\overline{I4}_2d)$ phase; red symbols represent the high-pressure scheelite-type $(I4_1/a)$ phase; squares represent the data collected at beamline 16-BM-D where Ne was used as the PTM; and circles represent the data collected at beamline 13-ID-D where KCl was used as the PTM. The dashed traces are the second-order Birch-Murnaghan EOS. 98 For the zircon-type structure, it was fitted from 0.2 to 14.5 GPa, using the data collected with both PTM. For the HPLS structure, it was fitted from 15.1 to 18.5 GPa, using the data collected with Ne as the PTM. For the scheelite-type structure, it was fitted from 4.1 to 28.6 GPa, using data only collected with KCl as the PTM.

400 different CeSiO₄ phases from the experiments and the fits of 401 the second-order Birch-Murnaghan EOS. 97 The equation 402 describing the second-order Birch-Murnaghan EOS is the 403 following:

$$P = \frac{3K_0}{2} \left[\left(\frac{V_0}{V} \right)^{7/3} - \left(\frac{V_0}{V} \right)^{5/3} \right] \tag{1}$$

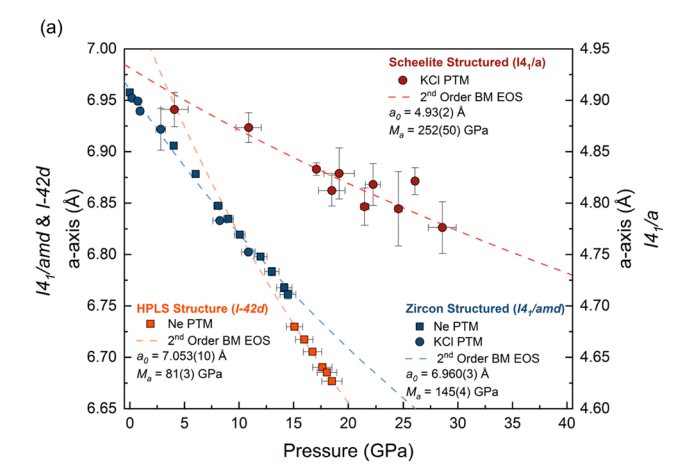
405 in which V_0 is the zero-pressure unit cell volume, V is the cell 406 volume at a given pressure (P), and K_0 is bulk modulus.⁹⁷ The 407 fits were performed with the EosFit7 software. The program 408 offers the possibility to use the uncertainties of the data points

to derive a weighting scheme for the fit. The errors associated 409 with both the measured pressure by ruby luminescence 62 and 410 the derived lattice parameters are from the Rietveld analyses. 411 While other studies on zircon-structured orthosilicates, such as 412 the work of Ehlers et al., 99 have used higher-ordered Birch- 413 Murnaghan EOS to fit their experimental data, it was not 414 needed in our work. When transforming the P-V data into 415 Eulerain strain (f_E) and a normalized stress, also referred to as 416 normalized pressure (F_E) , the data plots reasonably well along 417 a horizonal line (Figure S5). 100 This indicates that the data can 418 be fitted to a second-order Birch-Murnaghan EOS with 419 reasonable confidence.

The fits performed on the zircon-structured polymorph used 421 the data collected from 0.2 \pm 0.2 to 14.5 \pm 0.7 GPa and 422 applied the data collected from both sets of experiments 423 (Figure 4). The resulting fit to the second-order Birch- 424 Murnaghan EOS yielded a V_0 of 300.8(3) Å³ and a K_0 of 425 171(5) GPa. The derived V_0 (300.8(3) Å³) from the fitting 426 was in good agreement with the previously reported unit cell 427 volumes of the zircon-structured polymorph by Estevenon et 428 al. $(299.53(1) \text{ Å}^3)$, 55 Estevenon et al. $(299.85(2) \text{ Å}^3)$, 56 and 429 Strzelecki et al. (300.47(4) Å³).⁵⁹ At higher pressures, we 430 applied second-order Birch-Murnaghan EOS fitting on 431 scheelite-structure polymorph, using the decompression data 432 collected between 28.6 and 4.1 GPa from only the in situ high- 433 pressure laser-heated experiments, from which we yielded a $V_0\,$ 434 of 276(3) $Å^3$ and a K_0 of 221(40) GPa (Figure 4).

If the zircon structure was used between 15 and 19 GPa for 436 Rietveld analysis, it resulted in a deviation to lower-than- 437 expected volumes (Figure S6). This indicates that, at these 438 pressures, CeSiO₄ structure is undergoing a considerable 439 amount of softening. Such behavior is similar to what was 440 found by Van Western et al. when synthetically pure zircon was 441 compressed above 19.7 GPa. 101 Stangarone et al. argued that 442 the deviation to smaller volumes observed by Van Westrenen 443 et al. was a consequence of the displacive phase transition to 444 the HPLS phase. 22 This is also the rational basis on which we 445 assumed that CeSiO₄ might have undergone the HPLS phase 446 transition in this pressure region and used the HPLS structure 447 (space group: $\overline{I4}_2d$) to analyze the XRD data collected between 448 15 and 19 GPa (Figures 4 and S6). Applying a second-order 449 Birch-Murnaghan EOS fitting yielded a V_0 of 309(1) Å³ and a 450 K_0 of 105(4) GPa for the HPLS CeSiO₄, reflecting a softer 451 bulk modulus than the zircon-structure phase at lower 452 pressures. This lattice softening may signify an intermediate 453 nature of the HPLS phase between zircon and scheelite and 454 sequentially trigger the transition to the latter. If one believes 455 the argument of Stangarone et al. and fits the P-V data of Van 456 Westrenen et al., 101 for zircon from 19.66 to 22.16 GPa to a 457 second-order Birch-Murnaghan EOS, it yields a V_0 of 288(17) 458 ${\rm \AA}^3$ and a K_0 of 72(30) GPa, which again show a softening of 459 the bulk modulus for potentially a HPLS-structured material. 460

In order to further evaluate the validity of our derived K_0 461 and V_0 , we employed two verification methods. The first 462 method of verification is based on fitting unit cell parameters a 463 and c to a one-dimensional form of the Birch-Murnaghan 464 EOS (Figure 5). This was accomplished by replacing the V 465 f5 term with a^3 or c^3 and V_0 with a_0^3 or c_0^3 in eq 1 to yield values 466 for a_0 , M_a , c_0 , and M_c . The variables, M_a and M_c are respectively 467 the axial linear moduli of the a and c axes. The values derived 468 for M_a and M_c were used to further check the previously 469 derived K_0 and give confidence in these values through the 470 following relation:



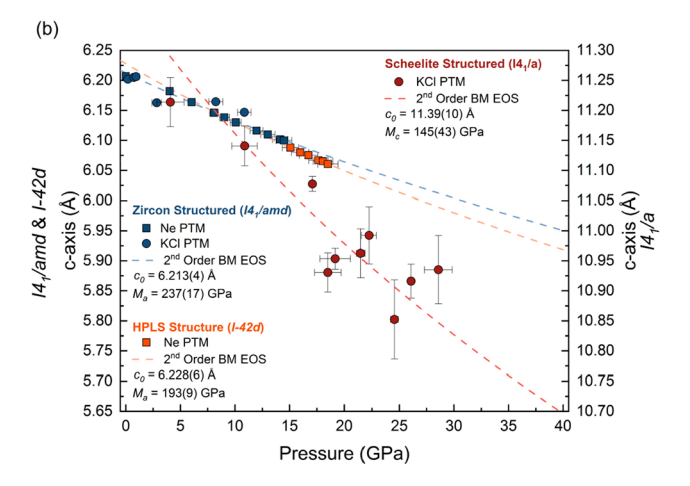


Figure 5. Unit cell parameters of $CeSiO_4$ as a function of pressure. (a) Variation in the a-axis and (b) variation in the c-axis for each of the phases. Blue symbols represent the low-pressure zircon-type $(I4_1/amd)$ phase; orange symbols represent the intermediate-pressure HPLS-type $(I4_2/a)$ phase; red symbols represent the high-pressure scheelite-type $(I4_1/a)$ phase; squares represent the data collected at beamline 16-BM-D where Ne was used as the PTM; and circles represent the data collected at beamline 13-ID-D where KCl was used as the PTM. The dashed traces are the second-order Birch–Murnaghan EOS: 98 for zircon type, this was fit from 0.2 to 10.1 GPa, using the data collected with both PTM; for the HPLS, this was fit from 15.1 to 18.5 GPa, using the data collected with Ne as the PTM; and for the scheelite-type, it was fitted from 4.1 to 28.6 GPa, using data only collected with KCl as the PTM.

$$K_{0,lm} = 3 \left(\frac{1}{M_a} + \frac{1}{M_a} + \frac{1}{M_c} \right)^{-1}$$
 (2)

473 For stetindite, the one-dimensional form of the Birch—474 Murnaghan EOS yielded $a_0 = 6.960(3)$ Å, $M_a = 145(4)$ 475 GPa, $c_0 = 6.213(4)$ Å, and $M_c = 237(17)$ GPa. Using the values 476 of a_0 and c_0 , $V_{0,lm}$ was calculated to be 300.8(3) Å³, in good 477 agreement with the unit cell volume V_0 of 301.0(3) Å³ (Figure 478 4). $K_{0,lm}$ was calculated by taking the derived values of M_a and 479 M_c into eq 2 to be 166(4) GPa, again in good agreement with 480 K_0 of 171(5) GPa from the volumetric data. Applying the one-481 dimensional Birch—Murnaghan EOS to data of HPLS phase 482 yielded the following values: $a_0 = 7.053(10)$ Å, $M_a = 81(3)$ 483 GPa, $c_0 = 6.228(6)$ Å, and $M_c = 193(9)$ GPa. $V_{0,lm}$ of HPLS

was calculated to be 309.8(9) ų, in agreement with V_0 of 484 309(1) ų. The derived $K_{0,lm}$ of HPLS, 101(3) GPa, also 485 agreed within error with K_0 of 105(4) GPa. Lastly, the 486 scheelite phase has the following values fitted from the one- 487 dimensional Birch–Murnaghan EOS: $a_0=4.93(2)$ Å, $M_a=488$ 252(50) GPa, $c_0=11.39(10)$ Å, and $M_c=145(43)$ GPa. $V_{0,lm}$ 489 of scheelite was evaluated to be 277(3) ų, which agreed with 490 V_0 of 276(3) ų. The derived $K_{0,lm}$ of scheelite, 202(35) GPa, 491 also agreed within error with K_0 of 221(40) GPa.

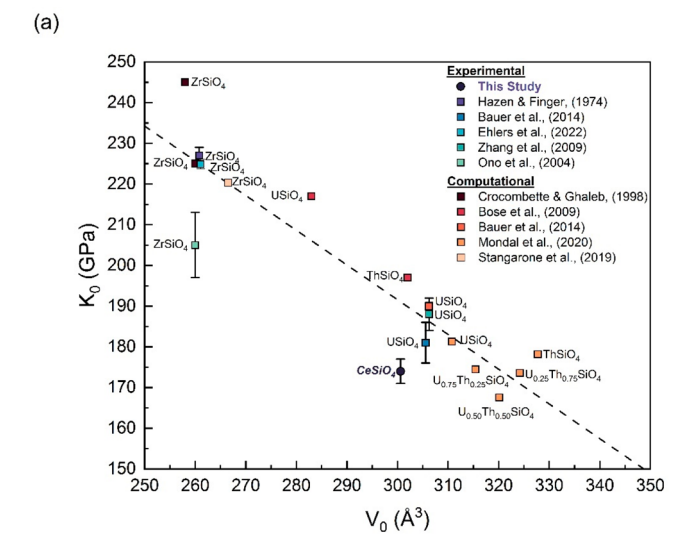
Through the first verification method, it was possible to gain 493 anisotropic insight into how the three polymorphs respond to 494 pressure. For the low-pressure zircon-structured polymorph, 495 the linear modulus along the c-axis (M_c = 237(17) GPa) is 1.63 496 \pm 0.13 times that along the a-axis ($M_a = 145(4)$ GPa), 497 suggesting more compressibility along the a-axis. The 498 anisotropic behavior can be explained by the arrangement of 499 TO₄ tetrahedra and MO₈ dodecahedra (Figure 1a,b). The 500 MO₈ dodecahedra can be depicted as two intersected 501 disphenoidal MO₄ forms: edge-sharing MO1₄ alternating 502 with TO₄ along the c-axis, and MO2₄ corner-sharing with 503 another MO24 tetrahedra forming a zigzagging chain along the 504 a-axis (Figure 1a,b). 2,102,103, Higher freedom of corner-sharing 505 MO2₄ tetrahedra makes the zircon structure more flexible 506 along the a-axis during compression, while the edge-sharing 507 rigid TO₄ arranging along the c-axis is less compressible. 103,104 508 Thus, due to the higher repulsion experienced due to the edge 509 sharing over corner sharing, the c-axis contracts at a slower rate 510 than that of the *a*-axis.

Because of the similarity in structure, the HPLS phase is also 512 more compressible along the a-axis than the c-axis, with the 513 degree of anisotropy further increased. This is evidenced by the 514 linear moduli of HPLS along the c-axis ($M_c = 193(9)$ GPa) is 515 2.38 times that along the a-axis ($M_a = 81(3)$ GPa). Such an 516 increase in anisotropic behavior can be explained by the 517 rotation of the SiO₄ tetrahedra around the c-axis. Due to this 518 symmetric operation with respect to the zircon structure, there 519 is an addition SiO₄-MO₈-SiO₄ edge-sharing chain that is 520 formed and the number of [001] channels increased from 2 to 521 4 per unit cell (Figure 1). As stated previously, for the zircon 522 structure these chains cause the anisotropic compressibility 523 behavior; therefore, an increase in the number of these 524 moieties in the unit cell would be expected to promote 525 anisotropy. Moreover, the increase in the degree of corner 526 sharing along the a-axis (Figure 1c,d) is the reason for the 527 dramatic decrease in the bulk moduli of the HPLS phase with 528 respect to stetindite.

After the second phase transformation, the high-pressure 530 scheelite-structured polymorph has an inverse anisotropic 531 behavior that is more compressible along the c-axis than the a- 532 axis, similar to the anisotropic behavior that was found for 533 synthetic reidite $(M_c/M_a = \sim 1.5)$. This is shown by the 534 linear modulus along the a-axis $(M_a = 252(50) \text{ GPa})$ is $1.73 \pm 535 = 0.61$ times than that along the c-axis $(M_c = 145(43) \text{ GPa})$. The 536 anisotropic behavior arises from the arrangement of the MO₈ 537 dodecahedra which form an edge-sharing chain that zigzags 538 along the a-axis. These chains are then cross-linked by the 539 TO₄ tetrahedra corner sharing with the MO₈ dodecahedra 540 parallel to the c-axis (Figure 1e,f). Subsequently, it is the 541 corner sharing parallel to the c-axis that gives rise to the 542 anisotropic compression. While such anisotropic behavior is 543 the inverse to what was found for both the zircon structured 544 and HPLS polymorphs, the mechanism of the prevalence of 545

546 edge-sharing moieties in a specific crystallographic direction 547 being the root cause of anisotropy is the same.

The second verification method is based on the empirical 549 inverse relationship between bulk modulus and unit cell 550 volume of isostructural inorganic materials. 107,108 Considering 551 that the bulk modulus of a given material is dictated by the 552 bulk moduli of its constituent polyhedra and their arrange-553 ment, 109 then the inverse relationship for isostructural 554 inorganic compounds (having the same polyhedra arrange-555 ment) is only dictated by the bulk moduli of polyhedra. Then, 556 obviously, the bulk modulus of polyhedron is inversely correlated with the ionic radius of its metal center as a result 558 of electrostatic interactions (i.e., repulsive forces). 107,109-111 559 This has been demonstrated at length for simple (i.e., MgO s60 and Al_2O_3) and complex oxides (i.e., $MgAl_2O_4$). 107,110,111 This 561 verification method could only be applied to the zircon and 562 scheelite structure polymorphs as there is no other study on 563 bulk moduli of comparable HPLS polymorphs. The derived 564 values for zircon are in good agreement with the empirically 565 derived trends of isostructural silicates (Figure 566 6). 4,8,9,23,25,112-114 Similarly for the high-pressure scheelite-



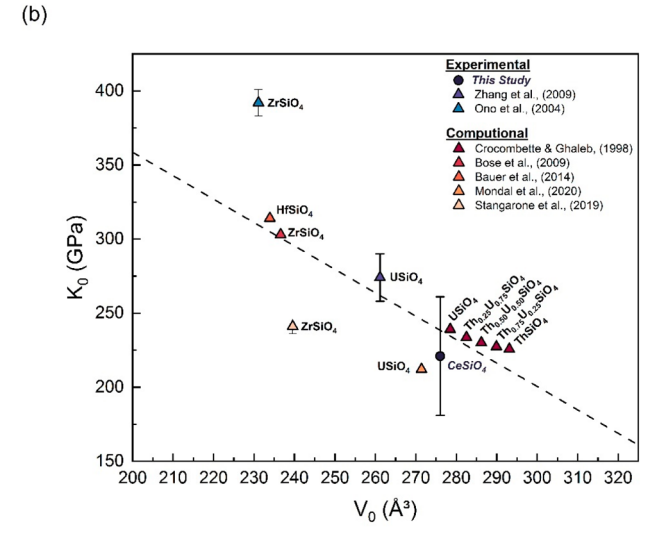


Figure 6. Comparison of bulk moduli of (a) zircon-type and (b) scheelite-type orthosilicate minerals. $^{4,8,9,23,25,112-114}$

structured phase, the derived K_0 value 221(40) GPa agrees 567 with those of USiO₄ with its experimental values of 195(6) 568 GPa and computational values (density functional theory, 569 DFT) of 212(1) GPa reported by Bauer et al.⁹ Because eight- 570 coordinated U⁴⁺ (1.00 Å) and Ce⁴⁺ (0.97 Å) are much closer 571 in terms of ionic radii than those of Hf⁴⁺ (0.83 Å) and Zr⁴⁺ 572 (0.84 Å),⁴⁹ the solid state behavior of stetindite is expected to 573 be closer to coffinite than hafnon or zircon.

4.2. Grüneisen Parameter. The Raman peak positions as $_{575}$ a function of pressure for CeSiO $_{4}$ up to 18.2 GPa are displayed $_{576}$ in Figures 7 and 8. Due to the relatively low intensities of the $_{577}$ f $_{768}$ antisymmetric deformation (ν_{4}), it was not able to be $_{578}$ discerned from the background (Figure 3) and thus is not $_{579}$

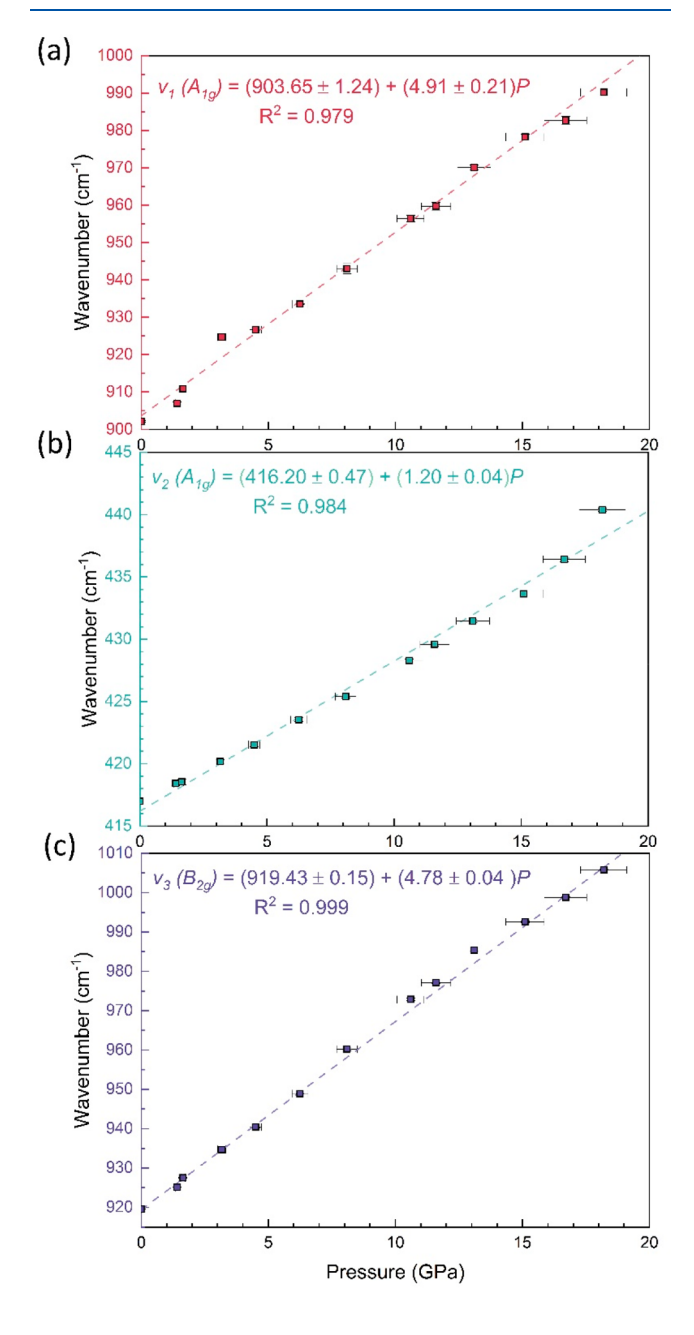


Figure 7. Pressure dependence of the internal Raman modes of stetindite from 0 to 18.2 GPa. (a) ν_1 (A_{1g}) SiO₄ symmetric stretching, (b) ν_2 (A_{1g}) SiO₄ symmetric bending, and (c) ν_3 (B_{2g}) SiO₄ antisymmetric stretching.

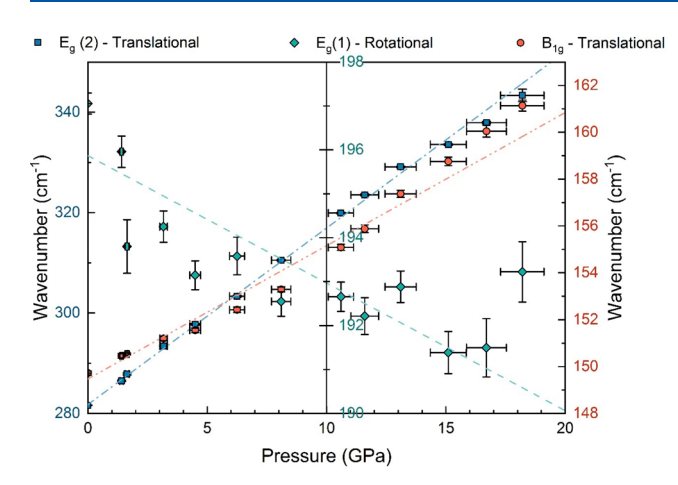


Figure 8. Pressure dependence of the external Raman modes of stetindite from 0 to 18.2 GPa.

580 included in Figure 7. The pressure derivatives of the peak positions $(d\nu/dP)$ up to 18.2 GPa were computed by linear fits 582 and are listed in Table 2. It is evident that all of the internal 583 vibrational modes of the [SiO₄] tetrahedron show positive 584 pressure dependence on the peak position (Figure 7). This 585 positive pressure dependence of the peak position is consistent 586 with decreasing the Si-O bond distances in the SiO₄ 587 tetrahedron. This behavior contrast what was found in 588 previous high-temperature Raman studies on CeSiO₄, where 589 a negative pressure derivative of the internal vibrational modes 590 due to an increasing of the Si-O bond distance of the SiO₄ so the to an increasing of the sternal modes, E_g (2) 592 and B_{1g}, were also found to have positive pressure derivatives 593 (Figure 8). However, the E_g (1) external mode exhibits a 594 negative pressure derivative until 15.1 GPa. The cause of this 595 negative pressure derivative is a result of the twisting of the 596 SiO₄ and CeO₈ polyhedra about the c-axis during the zircon to 597 HPLS phase transformation. The $E_g(1)$ mode then begins 598 to demonstrate some hardening above 15.1 GPa, as it begins to 599 demonstrate a positive pressure derivative (Figure 8). The 600 inflection point of the E_g (1) mode shifting from a negative 601 pressure derivative to a positive pressure derivative indicates 602 the transformation of the E_g (1) mode of the zircon structure 603 to an E mode of the HPLS-structured phase. 31 This behavior 604 of this lattice mode is consistent with that predicted by 605 Stangarone et al. and observed by Mihailova et al. in the zircon $606 \rightarrow \text{HPLS}$ phase transformation. ^{22,31} Overall, for stetindite, the 607 individual vibrational mode shifts $(d\nu/dP)$ are comparable to

those of other isostructural orthosilicate minerals (zircon, 608 hafnon, and coffinite), which are listed in Table 2.^{6,7,9} 609

Using the obtained K_0 value for stetindite (reported in the 610 previous section), in conjunction with vibrational mode shifts, 611 we have derived the mode Grüneisen parameters (γ_i) . γ_i were 612 derived through the following equation:

$$\gamma_i = \left(\frac{K_0}{\nu_0}\right) \left(\frac{\mathrm{d}\nu}{\mathrm{d}P}\right) \tag{3} _{614}$$

The derived values for the γ_i for stetindite are reported in 615 Table 2. Both the value of vibrational mode shifts and the bulk 616 modulus values are comparable to the other zircon-structure- 617 type orthosilicates, so are the γ_i . When comparing to other 618 nonzircon-type orthosilicate minerals, such as olivine ((Mg, 619 Fe)₂SiO₄), $^{115-117}$ garnet ((Mg, Ca, Fe)₃Al₂Si₃O₁₂) 118,119 and 620 aluminum silicate (Al₂SiO₅), 120 , we found that the obtained 621 pressure derivatives for the stretching and deformation modes 622 of the silica tetrahedra are comparable. Yet, they deviate from 623 these of γ_i . The reason for such a deviation in the γ_i between 624 the different orthosilicates is because the zircon-structure-type 625 are significantly less compressible, possessing higher K_0 values 626 than those of olivine and garnet, thus resulting in higher γ_i 627 values.

A similar procedure was applied to the high-pressure 629 scheelite-structure phase. The pressure derivatives of the 630 peak positions $(d\nu/dP)$ collected during the decompression 631 from 11.4 GPa to ambient were computed by linear fits. They 632 are listed in Table S8. It was found that all of the observable 633 vibrational modes show positive pressure derivatives. Using the 634 obtained K_0 value for the scheelite-structure phase, reported in 635 the previous section, in conjunction with available vibrational 636 mode shifts, we have derived the available γ_i using eq 3. These 637 γ_i are tabulated in Table S8.

5. CONCLUSIONS

In this work, we present the first high-pressure study on 639 synthetic stetindite by a combination of in situ high-pressure 640 synchrotron powder X-ray diffraction up 36.0 ± 1.8 GPa, in 641 situ high-pressure laser-heated synchrotron powder X-ray 642 diffraction up 28.6 ± 1.3 GPa and temperature more than 643 3000 K, and in situ high-pressure Raman spectroscopy up to 644 43.0 ± 2.2 GPa. High pressure in these experiments was 645 achieved by diamond anvil cells (DACs), with a variety of 646 different pressure transmitting media. The transition of zircon 647 to the HPLS phase was observed to occur at 15.1 GPa, 648 evidenced by the softening of elastic moduli. It should be 649

Table 2. Pressure Derivatives $(d\nu/dP)$ of the Vibrational Modes and Grüneisen Parameters (γ_i) of CeSiO₄ below 18.2 GPa and Comparison with the Values of Some Other Isostructural Minerals

	$d\nu_1/dP$ (cm ⁻¹ /GPa)	$\mathrm{d}\nu_2/\mathrm{d}P~(\mathrm{cm}^{-1}/\mathrm{GPa})$	$d\nu_3/dP$ (cm ⁻¹ /GPa)	$d\nu_4/dP$ (cm ⁻¹ /GPa)	Method	Ref
CeSiO ₄	4.9	1.2	4.8	N/A	Experimental	This Study
HfSiO ₄	4.1	1.1	4.6	N/A	Experimental	Manoun et al. ⁷
$ZrSiO_4$	4.1	1.1	4.8	N/A	Experimental	Knittle and Williams ⁶
USiO ₄	5.2	1.4	6.0	3.2	Experimental	Bauer et al. ⁹
USiO ₄	5.6	1.2	5.4	1.8	DFT	Bauer et al. ⁹
	γ_1	γ_2	γ_3	γ ₄ Method	od	Ref
CeSiO ₄	0.95	0.50	0.90 N	I/A Experim	ental	This Study
ZrSiO ₄	1.0	0.57	1.1 N	I/A Experim	ental	Knittle and Williams ⁶
USiO ₄	1.03	0.61	1.18 0	.99 Experim	Experimental	
$USiO_4$	1.12	0.54	1.07 0	.57 DFT		Bauer et al. ⁹

736

650 noted that the X-ray diffraction patterns of stetindite and 651 HPLS phase were nearly identical, due to only a minuscule 652 change in the symmetry between the $I4_1/amd$ and $\overline{I4}_2d$ space 653 groups. Besides the evidence from the softening in bulk 654 moduli, the emergence of the HPLS phase is supported by the 655 change in the pressure derivative of the E_g (1) mode from 656 negative to positive at 15.1 GPa, indicating its shifting from the 657 E_{σ} (1) mode of the zircon structure to an E mode of the HPLS 658 structure. The phase transition of HPLS to scheelite occurred 659 above 18.1 GPa. Scheelite is fully quenchable by means of 660 synchrotron powder X-ray diffraction and Raman spectrosco-661 py. The bulk moduli of stetindite, the HPLS, and the scheelite 662 structure phases were determined by fitting to a second-663 ordered Birch-Murnaghan EOS to be 171(5), 105(4), and 664 221(40) GPa, respectively. The pressure derivatives of the 665 vibrational modes of stetindite were consistent with those 666 previously reported for other orthosilicate minerals, including 667 pyrope (Mg₃Al₂ (SiO₄)₃, forsterite (Mg₂SiO₄), zircon, hafnon, and coffinite. The reported γ_i are in good agreement with those 669 reported for zircon, hafnon, and coffinite.

670 ASSOCIATED CONTENT

671 Supporting Information

672 The Supporting Information is available free of charge at 673 https://pubs.acs.org/doi/10.1021/acs.jpcc.2c06657.

PXRD, refined lattice parameters, in situ high-P Raman, 674 and equations of state (PDF) 675

676 AUTHOR INFORMATION

677 Corresponding Author

Xiaofeng Guo - Department of Chemistry, Washington State University, Pullman, Washington 99164, United States; 679 Alexandra Navrotsky Institute for Experimental 680 Thermodynamics and Materials Science and Engineering 681 Program, Washington State University, Pullman, Washington 682 99164, United States; orcid.org/0000-0003-3129-493X; 683 Email: x.guo@wsu.edu 684

685 Authors

694

695

696

697

698

699

700

701

702

703

704

705

706

Andrew Strzelecki - Department of Chemistry, Washington 686 State University, Pullman, Washington 99164, United States; 687 Alexandra Navrotsky Institute for Experimental 688 Thermodynamics and Materials Science and Engineering 689 Program, Washington State University, Pullman, Washington 690 99164, United States; Earth and Environmental Sciences 691 Division, Los Alamos National Laboratory, Los Alamos, New 692 Mexico 87545, United States 693

Xiaodong Zhao - Department of Chemistry, Washington State University, Pullman, Washington 99164, United States; Alexandra Navrotsky Institute for Experimental Thermodynamics, Washington State University, Pullman, Washington 99164, United States

Jason Baker – Earth and Environmental Sciences Division, Los Alamos National Laboratory, Los Alamos, New Mexico 87545, United States

Paul Estevenon – ICSM, University of Montpellier, CNRS, CEA, ENSCM, Bagnols sur Cèze 30207, France; CEA, DES, ISEC, DMRC, University of Montpellier, Bagnols sur Cèze 30207, France

Thomas Barral - ICSM, University of Montpellier, CNRS, CEA, ENSCM, Bagnols sur Cèze 30207, France

```
Adel Mesbah – ICSM, University of Montpellier, CNRS, CEA, 708
    ENSCM, Bagnols sur Cèze 30207, France; orcid.org/
    0000-0002-6905-2402
                                                              710
  Dmitry Popov - Advanced Photon Source, Argonne National 711
    Laboratory, Argonne, Illinois 60439, United States
                                                              712
  Stella Chariton - Center for Advanced Radiation Sources,
    University of Chicago, Chicago, Illinois 60439, United
                                                              714
    States; orcid.org/0000-0001-5522-0498
                                                              715
  Vitali Prakapenka – Center for Advanced Radiation Sources, 716
    University of Chicago, Chicago, Illinois 60439, United States 717
  Sohan Ahmed - Department of Chemistry, Washington State 718
    University, Pullman, Washington 99164, United States
                                                              719
  Choong-Shik Yoo – Department of Chemistry, Washington
                                                              720
    State University, Pullman, Washington 99164, United States; 721
    Materials Science and Engineering Program, Washington
                                                              722
    State University, Pullman, Washington 99164, United
                                                              723
    States; o orcid.org/0000-0002-2664-0730
                                                              724
  Nicolas Dacheux - ICSM, University of Montpellier, CNRS, 725
    CEA, ENSCM, Bagnols sur Cèze 30207, France;
                                                              726
    orcid.org/0000-0003-1636-1313
                                                              727
  Hongwu Xu – Earth and Environmental Sciences Division, Los 728
    Alamos National Laboratory, Los Alamos, New Mexico
                                                              729
    87545, United States; School of Molecular Sciences, and
                                                              730
    Center for Materials of the Universe, Arizona State
                                                              731
    University, Tempe Arizona 85287, United States
                                                              732
Complete contact information is available at:
                                                              733
https://pubs.acs.org/10.1021/acs.jpcc.2c06657
                                                              734
                                                              735
```

The authors declare no competing financial interest.

ACKNOWLEDGMENTS

737 This work was supported by the institutional funds from the 738 Department of Chemistry at Washington State University 739 (WSU) in the early stage, and later supported by the National 740 Science Foundation (NSF), Division of Materials Research, 741 under Award No. 2144792, and Division of Earth Sciences, 742 under Award No. 2149848. A.S. also acknowledges the 743 supported by the G. T. Seaborg Institute through a Summer 744 Research Fellowship. C.-S.Y. at WSU also acknowledges the 745 support by the NSF (DMR 2112653) and DOE-NNSA (DE-746 NA0003918). A portion of the research presented in this 747 article was supported by the Laboratory Directed Research and 748 Development (LDRD) program of Los Alamos National 749 Laboratory (LANL) under Project No. 20180007 DR. LANL, 750 an affirmative action/equal opportunity employer, is managed 751 by Triad National Security, LLC, for the National Nuclear 752 Security Administration of the U.S. Department of Energy 753 under Contract 89233218CNA000001. A portion of this work 754 was performed at HPCAT (Sector 16), Advanced Photon 755 Source (APS), Argonne National Laboratory. HPCAT 756 operations are supported by DOE-NNSA's Office of 757 Experimental Sciences. A portion of this work was performed 758 at GeoSoilEnviroCARS (The University of Chicago, Sector 759 13), Advanced Photon Source (APS), Argonne National 760 Laboratory. GeoSoilEnviroCARS is supported by the NSF- 761 Earth Sciences (EAR-1634415). This research used resources 762 of the Advanced Photon Source, a U.S. Department of Energy 763 (DOE) Office of Science User Facility operated for the DOE 764 Office of Science by Argonne National Laboratory under 765 Contract No. DE-AC02-06CH11357.

767 REFERENCES

- 768 (1) Speer, J. A. Zircon. Rev. Mineral. Geochem. **1980**, 5, 67–112.
- 769 (2) Finch, R. J.; Hanchar, J. M.; Zircon; Hanchar, J. M.; Hoskin, P. 770 W. O. Structure and Chemistry of Zircon and Zircon-Group Minerals. 771 *Rev. Mineral. Geochem.* **2003**, *53*, 1–26.
- 772 (3) Reid, A. F.; Ringwood, A. E. Newly Observed High Pressure 773 Transformation in Mn₃O₄, CaAl₂O4, and ZrSiO₄. *Earth Planet. Sci.* 774 *Lett.* **1969**, *6*, 205–208.
- 775 (4) Hazen, R. M.; Finger, L. M. Crystal Structure and 776 Compressibility of Zircon at High Pressure. *Am. Mineral.* **1979**, *64*, 777 196–201.
- 778 (5) Gucsik, A.; Zhang, M.; Koeberl, C.; Salje, E. K. H.; Redfern, S. A. 779 T.; Pruneda, J. M. Infrared and Raman Spectra of $ZrSiO_4$ 780 Experimentally Shocked at High Pressures. *Mineral. Mag.* **2004**, 68 781 (5), 801–811.
- 782 (6) Knittle, E.; Williams, Q. High-Pressure Raman Spectroscopy of 783 ZrSiO₄: Observation of the Zircon to Scheelite Transition at 300 K. 784 Am. Mineral. **1993**, 78 (3–4), 245–252.
- 78S (7) Manoun, B.; Downs, R. T.; Saxena, S. K. A High-Pressure 786 Raman Spectroscopic Study of Hafnon, HfSiO₄. Am. Mineral. **2006**, 787 91 (11–12), 1888–1892.
- 788 (8) Zhang, F. X.; Pointeau, V.; Shuller, L. C.; Reaman, D. M.; Lang, 789 M.; Liu, Z.; Hu, J.; Panero, W. R.; Becker, U.; Poinssot, C.; Ewing, R. 790 C. Structural Transitions and Electron Transfer in Coffinite, USiO₄, at 791 High Pressure. *Am. Mineral.* **2009**, *94* (7), 916–920.
- 792 (9) Bauer, J. D.; Labs, S.; Weiss, S.; Bayarjargal, L.; Morgenroth, W.; 793 Milman, V.; Perlov, A.; Curtius, H.; Bosbach, D.; Zänker, H.; Winkler, 794 B. High-Pressure Phase Transition of Coffinite, USiO₄. *J. Phys. Chem.* 795 *C* 2014, *118* (43), 25141–25149.
- 796 (10) Zhang, F. X.; Lang, M.; Ewing, R. C.; Lian, J.; Wang, Z. W.; Hu, 797 J.; Boatner, L. A. Pressure-Induced Zircon-Type to Scheelite-Type 798 Phase Transitions in YbPO₄ and LuPO₄. *J. Solid State Chem.* **2008**, 799 181 (10), 2633–2638.
- 800 (11) Lacomba-Perales, R.; Errandonea, D.; Meng, Y.; Bettinelli, M. 801 High-Pressure Stability and Compressibility of APO₄ (A = La, Nd, Eu, 802 Gd, Er, and Y) Orthophosphates: An x-Ray Diffraction Study Using 803 Synchrotron Radiation. *Phys. Rev. B Condens. Matter Mater. Phys.* 804 **2010**, 81 (6), 1–9.
- 805 (12) López-Solano, J.; Rodríguez-Hernández, P.; Muñoz, A.; Gomis, 806 O.; Santamaría-Perez, D.; Errandonea, D.; Manjón, F. J.; Kumar, R. S.; 807 Stavrou, E.; Raptis, C. Theoretical and Experimental Study of the 808 Structural Stability of TbPO₄ at High Pressures. *Phys. Rev. B* 809 *Condens. Matter Mater. Phys.* **2010**, 81 (14), 1–9.
- 810 (13) Gomis, O.; Lavina, B.; Rodríguez-Hernández, P.; Muñoz, A.; 811 Errandonea, R.; Errandonea, D.; Bettinelli, M. High-Pressure 812 Structural, Elastic, and Thermodynamic Properties of Zircon-Type 813 HoPO₄ and TmPO₄. *J. Phys.: Condens. Matter* **2017**, 29 (9), 095401. 814 (14) Heuser, J. M.; Palomares, R. I.; Bauer, J. D.; Rodriguez, M. J. L.; 815 Cooper, J.; Lang, M.; Scheinost, A. C.; Schlenz, H.; Winkler, B.; 816 Bosbach, D.; et al. Structural Characterization of (Sm, Tb) PO₄ Solid 817 Solutions and Pressure-Induced Phase Transitions. *J. Eur. Ceram. Soc.*
- 819 (15) Wang, X.; Loa, I.; Syassen, K.; Hanfland, M.; Ferrand, B. 820 Structural Properties of the Zircon- and Scheelite-Type Phases of 821 YVO₄ at High Pressure. *Phys. Rev. B* **2004**, *70* (6), 064109.

818 2018, 38 (11), 4070-4081.

- 822 (16) Errandonea, D.; Kumar, R. S.; Achary, S. N.; Tyagi, A. K. In 823 Situ High-Pressure Synchrotron x-Ray Diffraction Study of CeVO₄ 824 and TbVO₄ up to 50 GPa. *Phys. Rev. B Condens. Matter Mater. Phys.* 825 **2011**, 84 (22), 1–8.
- 826 (17) Huang, Z.; Zhang, L.; Pan, W. Synthesis, Lattice Dynamics, and 827 Mechanical Properties of a High-Pressure Scheelite Phase of RVO₄. 828 *Inorg. Chem.* **2012**, *51* (21), 11235–11237.
- 829 (18) Errandonea, D.; Popescu, C.; Achary, S. N.; Tyagi, A. K.; 830 Bettinelli, M. In Situ High-Pressure Synchrotron X-Ray Diffraction 831 Study of the Structural Stability in NdVO₄ and LaVO₄. *Mater. Res.* 832 *Bull.* **2014**, *50*, 279–284.
- 833 (19) Panchal, V.; Errandonea, D.; Manjón, F. J.; Muñoz, A.; 834 Rodríguez-Hernández, P.; Bettinelli, M.; Achary, S. N.; Tyagi, A. K.

- High Pressure Phase Transitions in NdVO₄. AIP Conf. Proc. 2015, 835 1665, 030006.
- (20) Garg, A. B.; Errandonea, D. High-Pressure Powder x-Ray 837 Diffraction Study of EuVO₄. *J. Solid State Chem.* **2015**, 226, 147–153. 838
- (21) Ruiz-Fuertes, J.; Martínez-García, D.; Marqueño, T.; 839 Errandonea, D.; Macleod, S. G.; Bernert, T.; Haussühl, E.; 840 Santamaría-Pérez, D.; Ibáñez, J.; Mallavarapu, A.; et al. High-Pressure 841 High-Temperature Stability and Thermal Equation of State of Zircon-842 Type Erbium Vanadate. *Inorg. Chem.* 2018, 57 (21), 14005–14012. 843
- (22) Stangarone, C.; Angel, R. J.; Prencipe, M.; Mihailova, B.; 844 Alvaro, M. New Insights into the Zircon-Reidite Phase Transition. 845 Am. Mineral. 2019, 104 (6), 830–837.
- (23) Luo, W.; Ahuja, R. High Pressure Structural Phase Transition 847 in Zircon (ZrSiO₄). J. Phys. Conf. Ser. 2008, 121, 0220014.
- (24) Bose, P. P.; Mittal, R.; Chaplot, S. L. Lattice Dynamics and 849 High Pressure Phase Stability of Zircon Structured Natural Silicates. 850 Phys. Rev. B Condens. Matter Mater. Phys. 2009, 79 (17), 1–8.
- (25) Tange, Y.; Takahashi, E. Stability of the High-Pressure 852 Polymorph of Zircon ($ZrSiO_4$) in the Deep Mantle. *Phys. Earth* 853 *Planet. Inter.* **2004**, 143 (1–2), 223–229.
- (26) Ono, S.; Tange, Y.; Katayama, I.; Kikegawa, T. Equation of 855 State of ZrSiO₄ Phases in the Upper Mantle. *Am. Mineral.* **2004**, 89, 856 185–188.
- (27) Ono, S.; Funakoshi, K.; Nakajima, Y.; Tange, Y.; Katsura, T. 858 Phase Transition of Zircon at High P-T Conditions. *Contrib. to* 859 *Mineral. Petrol.* **2004**, 147 (4), 505–509.
- (28) Farnan, I.; Balan, E.; Pickard, C. J.; Mauri, F. The Effects of 861 Radiation on Local Structure in the Crystalline Fraction of ZrSiO₄: 862 Investigating the 29Si NMR Response to Pressure in Zircon and 863 Reidite. Am. Mineral. 2003, 88, 1663–1667.
- (29) Glass, B. P.; Liu, S.; Leavens, P. B. Reidite: An Impact- 865 Produced High-Pressure Polymorph of Zircon Found in Marine 866 Sediments. *Am. Mineral.* **2002**, *87* (4), 562–565.
- (30) Du, J.; Devanathan, R.; RenéCorrales, L.; Weber, W. J. First-868 Principles Calculations of the Electronic Structure, Phase Transition 869 and Properties of ZrSiO₄ Polymorphs. *Comput. Theor. Chem.* **2012**, 870 987, 62–70.
- (31) Mihailova, B.; Waeselmann, N.; Stangarone, C.; Angel, R. J.; 872 Prencipe, M.; Alvaro, M. The Pressure-Induced Phase Transition(s) 873 of ZrSiO₄: Revised: Experimental Proof for the Existence of a New 874 High-Pressure Polymorph of Zircon. *Phys. Chem. Miner.* **2019**, 46 (8), 875 807–814.
- (32) Ewing, R. C.; Wang, L. M. Phosphates as Nuclear Waste Forms. 877 In *Phosphates: Geochemical, Geobiological and Materials Importance*; 878 Kohn, M. J., Rakovan, J., Hughes, J. M., Eds.; Mineralogical Society of 879 America, 2002; Vol. 48, pp 673–700. DOI: 10.2138/rmg.2002.48.18. 880
- (33) Boatner, L. A. Synthesis, Structure, and Properties of Monazite, 881 Pretulite, and Xenotime. *Reviews in Mineralogy and Geochemistry* **2002**, 882 48, 87–121.
- (34) Orlova, A. I.; Ojovan, M. I. Ceramic Mineral Waste-Forms for 884 Nuclear Waste Immobilization. *Materials (Basel)*. **2019**, 12 (16), 885 2638.
- (35) Rafiuddin, M. R.; Grosvenor, A. P. Probing the Effect of 887 Radiation Damage on the Structure of Rare-Earth Phosphates. *J.* 888 Alloys Compd. **2015**, 653, 279–289.
- (36) Boatner, L. A.; Abraham, M. M.; Sales, B. C. Lanthanide 890 Orthophosphate Ceramics for the Disposal of Actinide-Contaminated 891 Nuclear Wastes. *Inorg. Chim. Acta* **1984**, 94 (1–3), 146–148.
- (37) Lumpkin, G. R. Ceramic Waste Forms for Actinides. *Elements* 893 **2006**, 2 (6), 365–372.
- (38) Ewing, R. C.; Lutze, W.; Weber, W. J. Zircon: A Host-Phase for 895 the Disposal of Weapons Plutonium. *J. Mater. Res.* **1995**, *10* (2), 243–896 246.
- (39) Guo, X.; Navrotsky, A.; Kukkadapu, R. K.; Engelhard, M. H.; 898 Lanzirotti, A.; Newville, M.; Ilton, E. S.; Sutton, S. R.; Xu, H. 899 Structure and Thermodynamics of Uranium-Containing Iron Garnets. 900 Geochim. Cosmochim. Acta 2016, 189, 269–281.
- (40) Guo, X.; Szenknect, S.; Mesbah, A.; Clavier, N.; Poinssot, C.; 902 Wu, D.; Xu, H.; Dacheux, N.; Ewing, R. C.; Navrotsky, A. Energetics 903

- 904 of a Uranothorite ($Th_{1-X}U_xSiO_4$) Solid Solution. Chem. Mater. **2016**, 905 28 (19), 7117–7124.
- 906 (41) Guo, X.; Tavakoli, A. H.; Sutton, S.; Kukkadapu, R. K.; Qi, L.; 907 Lanzirotti, A.; Newville, M.; Asta, M.; Navrotsky, A. Cerium 908 Substitution in Yttrium Iron Garnet: Valence State, Structure, and 909 Energetics. *Chem. Mater.* **2014**, 26 (2), 1133–1143.
- 910 (42) Chung, C. K.; O'Quinn, E. C.; Neuefeind, J. C.; Fuentes, A. F.; 911 Xu, H.; Lang, M.; Navrotsky, A. Thermodynamic and Structural 912 Evolution of Mechanically Milled and Swift Heavy Ion Irradiated 913 Er, Ti, O, Pyrochlore. *Acta Mater.* **2019**, *181*, 309–317.
- 914 (43) Helean, K. B.; Navrotsky, A.; Vance, E. R.; Carter, M. L.; 915 Ebbinghaus, B.; Krikorian, O.; Lian, J.; Wang, L. M.; Catalano, J. G. 916 Enthalpies of Formation of Ce-Pyrochlore, Ca_{0.93}Ce_{1.00}Ti_{2.035}O_{7.00}, U-917 Pyrochlore, Ca_{1.46}U⁴⁺_{0.23}U⁶⁺_{0.46}Ti_{1.85}O_{7.00} and Gd-Pyrochlore, 918 Gd₂Ti₂O₇: Three Materials Relevant to the Proposed Waste Form 919 for Excess Weapons Plutonium. *J. Nucl. Mater.* **2002**, 303 (2–3), 920 226–239.
- 921 (44) Neumeier, S.; Kegler, P.; Arinicheva, Y.; Shelyug, A.; Kowalski, 922 P. M.; Schreinemachers, C.; Navrotsky, A.; Bosbach, D. Thermo-923 chemistry of $La_{1-x}Ln_xPO_4$ -Monazites (Ln = Gd, Eu). *J. Chem.* 924 *Thermodyn.* **2017**, *105*, 396–403.
- 925 (45) Ewing, R. C. Nuclear Waste Forms for Actinides. *Proc. Natl.* 926 Acad. Sci. U. S. A. **1999**, 96 (7), 3432–3439.
- 927 (46) Ushakov, S. V.; Gong, W.; Yagokina, M. M.; Helean, K. B.; 928 Lutze, W.; Ewing, R. C. Solid Solutions of Ce, U, and Th in Zircon. 929 *Ceram. Trans.* **1999**, 93, 357–363.
- 930 (47) Keller, V. C. Untersuchungen Über Die Germanate Und 931 Silikate Des Typs ABO₄ Der Vierwertigen Elemente Thorium Bis 932 Americium. *Nukleonik* 1963, 5, 41–48.
- 933 (48) Estevenon, P.; Welcomme, E.; Tamain, C.; Jouan, G.; 934 Szenknect, S.; Mesbah, A.; Poinssot, C.; Moisy, P.; Dacheux, N. 935 Formation of PuSiO₄ under Hydrothermal Conditions. *Dalt. Trans.* 936 **2020**, *49*, 6434.
- 937 (49) Shannon, R. D. Revised Effective Ionic Radii and Systematic 938 Studies of Interatomic Distances in Halides and Chalcogenides. *Acta* 939 *Crystallogr., Sect. A* **1976**, 32 (5), 751–767.
- 940 (50) Zamoryanskaya, M. V.; Burakov, B. E. Feasibility Limits in 941 Using Cerium as a Surrogate for Plutonium Incorporation in Zircon, 942 Zirconia and Pyrochlore. *Mater. Res. Soc. Symp. Proc.* **2000**, *663*, 943 301–306.
- 944 (51) Putnam, R. L.; Navrotsky, A.; Cordfunke, E. H. P.; Huntelaar, 945 M. E. Thermodynamics of Formation of Two Cerium Aluminum 946 Oxides, CeAlO $_{3(s)}$ and CeAl $_{12}O_{19.918(s)}$, and Cerium Sesquioxide, 947 Ce $_2O_{3(s)}$ At T= 298.15 K. *J. Chem. Thermodyn.* **2000**, 32 (7), 911–948 921.
- 949 (52) Putnam, R. L.; Gallegos, U. F.; Ebbinghaus, B. B.; Navrotsky, 950 A.; Helean, K. B.; Ushakov, S. V.; Woodfield, B. F.; Boerio-Goates, J.; 951 Williamson, M. A. Formation Energetics of Ceramic Phases Related to 952 Surplus Plutonium Disposition, Report No. LA-UR-00-1960; Los 953 Alamos National Laboratory, 2000.
- 954 (53) Marra, J. C.; Cozzi, A. D.; Pierce, R. A.; Pareizs, J. M.; 955 Jurgensen, A. R.; Missimer, D. M. Cerium as a Surrogate in the 956 Plutonium Immobilized Form. In *Environmental Issues and Waste* 957 Management Technologies in the Ceramic and Nuclear Industries; Smith, 958 G. L., Sundaram, S. K., Spearing, D. R., Eds.; American Ceramic 959 Society, 2002; pp 381–388. DOI: 10.1002/9781118371435.ch36.
- 960 (54) Schlüter, J.; Malcherek, T.; Husdal, T. A. The New Mineral 961 Stetindite, CeSiO₄, a Cerium End-Member of the Zircon Group. 962 Neues Jahrb. fur Mineral. Abhandlungen **2009**, 186 (2), 195–200.
- 963 (55) Estevenon, P.; Welcomme, E.; Szenknect, S.; Mesbah, A.; 964 Moisy, P.; Poinssot, C.; Dacheux, N. Preparation of $CeSiO_4$ from 965 Aqueous Precursors under Soft Hydrothermal Conditions. *Dalt.* 966 *Trans.* **2019**, 48 (22), 7551–7559.
- 967 (56) Estevenon, P.; Kaczmarek, T.; Vadot, F.; Dumas, T.; Solari, P. 968 L.; Welcomme, E.; Szenknect, S.; Mesbah, A.; Moisy, P.; Poinssot, C.; 969 Dacheux, N. Formation of CeSiO₄ from Cerium (III) Silicate 970 Precursors. *Dalt. Trans.* **2019**, *48*, 10455–10463.
- 971 (57) Strzelecki, A. C.; Bourgeois, C.; Kriegsman, K. W.; Estevenon, 972 P.; Wei, N.; Szenknect, S.; Mesbah, A.; Wu, D.; Ewing, R. C.;

- Dacheux, N.; Guo, X. Thermodynamics of CeSiO₄: Implications for 973 Actinide Orthosilicates. *Inorg. Chem.* **2020**, *59* (18), 13174–13183. 974 (58) Strzelecki, A. C.; Kriegsman, K. W.; Estevenon, P.; Goncharov, 975 V.; Bai, J.; Szenknect, S.; Mesbah, A.; Wu, D.; McCloy, J. S.; Dacheux, 976 N.; Guo, X. High-Temperature Thermodynamics of Cerium Silicates, 977 A-Ce₂Si₂O₇ and Ce_{4.67} (SiO₄)₃O. *ACS Earth Space Chem.* **2020**, 4 978 (11), 2129–2143.
- (59) Strzelecki, A. C.; Barral, T.; Estevenon, P.; Mesbah, A.; 980 Goncharov, V.; Baker, J.; Bai, J.; Clavier, N.; Szenknect, S.; Migdissov, 981 A.; et al. The Role of Water and Hydroxyl Groups in the Structures of 982 Stetindite and Coffinite, $MSiO_4$ (M = Ce, U). *Inorg. Chem.* **2021**, *60*, 983 718–735.
- (60) Hrubiak, R.; Sinogeikin, S.; Rod, E.; Shen, G. The Laser Micro- 985 Machining System for Diamond Anvil Cell Experiments and General 986 Precision Machining Applications at the High Pressure Collaborative 987 Access Team. *Rev. Sci. Instrum.* **2015**, 86 (7), 072202. 988
- (61) Park, C.; Popov, D.; Ikuta, D.; Lin, C.; Kenney-Benson, C.; 989 Rod, E.; Bommannavar, A.; Shen, G. New Developments in Micro-X- 990 Ray Diffraction and X-Ray Absorption Spectroscopy for High- 991 Pressure Research at 16-BM-D at the Advanced Photon Source. 992 Rev. Sci. Instrum. 2015, 86 (7), 072205.
- (62) Mao, H. K.; Xu, J.; Bell, P. M. Calibration of the Ruby Pressure 994 Gauge to 800 Kbar under Quasi-Hydrostatic Conditions. *J. Geophys.* 995 Res. 1986, 91, 4673–4676.
- (63) Rivers, M.; Prakapenka, V. B.; Kubo, A.; Pullins, C.; Holl, C. 997 M.; Jacobsen, S. D. The COMPRES/GSECARS Gas-Loading System 998 for Diamond Anvil Cells at the Advanced Photon Source. *High Press.* 999 *Res.* 2008, 28 (3), 273–292.
- (64) Prescher, C.; Prakapenka, V. B. DIOPTAS: A Program for 1001 Reduction of Two-Dimensional X-Ray Diffraction Data and Data 1002 Exploration. *High Press. Res.* **2015**, *35* (3), 223–230.
- (65) Toby, B. H.; Von Dreele, R. B. GSAS-II: The Genesis of a 1004 Modern Open-Source All Purpose Crystallography Software Package. 1005 *J. Appl. Crystallogr.* **2013**, *46* (2), 544–549.
- (66) Chidester, B. A.; Thompson, E. C.; Fischer, R. A.; Heinz, D. L.; 1007 Prakapenka, V. B.; Meng, Y.; Campbell, A. J. Experimental Thermal 1008 Equation of State of B2-KCl. *Phys. Rev. B* **2021**, *104* (9), 5–10.
- (67) Lin, J. F.; Struzhkin, V. V.; Jacobsen, S. D.; Shen, G.; 1010 Prakapenka, V. B.; Mao, H. K.; Hemley, R. J. X-Ray Emission 1011 Spectroscopy with a Laser-Heated Diamond Anvil Cell: A New 1012 Experimental Probe of the Spin State of Iron in the Earth's Interior. J. 1013 Synchrotron Radiat. 2005, 12 (5), 637–641.
- (68) Shen, G.; Wang, Y.; Prakapenka, V.; Benmore, C. J.; Alp, E. E.; 1015 Ding, Y.; Yang, W. High-Pressure Research at the Advanced Photon 1016 Source. *Synchrotron Radiat. News* **2010**, 23 (3), 32–38.
- (69) Prakapenka, V. B.; Kubo, A.; Kuznetsov, A.; Laskin, A.; 1018 Shkurikhin, O.; Dera, P.; Rivers, M. L.; Sutton, S. R. Advanced Flat 1019 Top Laser Heating System for High Pressure Research at GSECARS: 1020 Application to the Melting Behavior of Germanium. *High Press. Res.* 1021 2008, 28 (3), 225–235.
- (70) Dewaele, A.; Belonoshko, A. B.; Garbarino, G.; Occelli, F.; 1023 Bouvier, P.; Hanfland, M.; Mezouar, M. High-Pressure-High-Temper- 1024 ature Equation of State of KCl and KBr. *Phys. Rev. B Condens. Matter* 1025 *Mater. Phys.* 2012, 85 (21), 1–7.
- (71) Zha, C. S.; Mibe, K.; Bassett, W. A.; Tschauner, O.; Mao, H. K.; 1027 Hemley, R. J. P-V-T Equation of State of Platinum to 80 GPa and 1028 1900 K from Internal Resistive Heating/X-Ray Diffraction Measurements. J. Appl. Phys. 2008, 103 (5), 054908.
- (72) Kalintsev, A.; Migdisov, A.; Alcorn, C.; Baker, J.; Brugger, J.; 1031 Mayanovic, R. A.; Akram, N.; Guo, X.; Xu, H.; Boukhalfa, H.; et al. 1032 Uranium Carbonate Complexes Demonstrate Drastic Decrease in 1033 Stability at Elevated Temperatures. *Commun. Chem.* 2021, 4 (1), 120. 1034 (73) Strzelecki, A. C.; Reece, M. E.; Zhao, X.; Yu, W.; Benmore, C. 1035
- J.; Ren, Y.; Alcorn, C. D.; Migdisov, A.; Xu, H.; Guo, X. 1036 Thermodynamics of Mixing HREE in Xenotime Solid Solution 1037 (Er_(x)Yb_(1-x)PO₄). ACS Earth Space Chem. **2022**, *6*, 1375–1389.
- (74) Klotz, S.; Chervin, J. C.; Munsch, P.; Le Marchand, G. 1039 Hydrostatic Limits of 11 Pressure Transmitting Media. J. Phys. D. 1040 Appl. Phys. 2009, 42 (7), 075413.

- 1042 (75) Kamb, B. Structure of Ice VI. Science (80-.). **1965**, 150 (10), 1043 205–209.
- 1044 (76) Chen, J. Y.; Yoo, C. S. High Density Amorphous Ice at Room 1045 Temperature. *Proc. Natl. Acad. Sci. U. S. A.* **2011**, *108* (19), 7685—1046 7688.
- 1047 (77) Salzmann, C. G. Advances in the Experimental Exploration of 1048 Water's Phase Diagram. *J. Chem. Phys.* **2019**, *150* (6), 060901.
- 1049 (78) Bina, C. R.; Navrotsky, A. Possible Presence of High-Pressure 1050 Ice in Cold Subducting Slabs. *Nature* **2000**, 408 (6814), 844–847.
- 1051 (79) Gillet, P.; Malézieux, J. M.; Itié, J. P. Phase Changes and 1052 Amorphization of Zeolites at High Pressures: The Case of Scolecite 1053 and Mesolite. *Am. Mineral.* **1996**, *81* (5–6), 651–657.
- 1054 (80) Zhu, J.; Quan, Z.; Lin, Y. S.; Jiang, Y. B.; Wang, Z.; Zhang, J.; 1055 Jin, C.; Zhao, Y.; Liu, Z.; Brinker, C. J.; Xu, H. Porous Ice Phases with 1056 VI and Distorted VII Structures Constrained in Nanoporous Silica. 1057 Nano Lett. 2014, 14 (11), 6554–6558.
- 1058 (81) Errandonea, D.; Garg, A. B. Recent Progress on the 1059 Characterization of the High-Pressure Behaviour of AVO₄ Orthova-1060 nadates. *Prog. Mater. Sci.* **2018**, *97* (April), 123–169.
- 1061 (82) Dawson, P.; Hargreave, M. M.; Wilkinson, G. R. The 1062 Vibrational Spectrum of Zircon ($ZrSiO_4$). *J. Phys. C Solid State* 1063 *Phys.* **1971**, 4 (2), 240–256.
- 1064 (83) Clavier, N.; Szenknect, S.; Costin, D. T.; Mesbah, A.; Poinssot, 1065 C.; Dacheux, N. From Thorite to Coffinite: A Spectroscopic Study of 1066 Th_{1-X}U_xSiO4 Solid Solutions. Spectrochim. Acta Part A Mol. Biomol. 1067 Spectrosc. **2014**, 118, 302–307.
- 1068 (84) Kolesov, B. A.; Geiger, C. A.; Armbruster, T. The Dynamic 1069 Properties of Zircon Studied by Single-Crystal X-Ray Diffraction and 1070 Raman Spectroscopy. *Eur. J. Mineral.* **2001**, *13* (5), 939–948.
- 1071 (85) Hoskin, P. W. O.; Rodgers, K. A. Raman Spectral Shift in the 1072 Isomorphous $(Zr_{1-X}Hf_x)$ SiO₄. Eur. J. Solid State Inorg. Chem. **1996**, 33 1073 (11), 1111–1121.
- 1074 (86) Nasdala, L. Spectroscopic Methods Applied to Zircon. *Rev.* 1075 *Mineral. Geochem.* **2003**, 53, 427–467.
- 1076 (87) Syme, R. W. G.; Lockwood, D. J.; Kerr, H. J. Raman Spectrum 1077 of Synthetic Zircon (ZrSiO₄) and Raman Spectrum of Synthetic 1078 Zircon (ZrSiO₄) and Thorite. *Solid State Phys.* **1977**, *10*, 1335–1348.
- 1079 (88) Geisler, T.; Burakov, B. E.; Zirlin, V.; Nikolaeva, L.; Pöml, P. A 1080 Raman Spectroscopic Study of High-Uranium Zircon from the 1081 Chernobyl "Lava. Eur. J. Mineral. 2006, 17 (6), 883–894.
- 1082 (89) Manjón, F. J.; Errandonea, D.; Garro, N.; Pellicer-Porres, J.; 1083 Rodríguez-Hernández, P.; Radescu, S.; López-Solano, J.; Mujica, A.; 1084 Muñoz, A. Lattice Dynamics Study of Scheelite Tungstates under 1085 High Pressure I. BaWO₄. *Phys. Rev. B Condens. Matter Mater. Phys.* 1086 **2006**, 74 (14), 1–17.
- 1087 (90) Manjon, F. J.; Errandonea, D.; Garro, N.; Pellicer-Porres, J.; 1088 López-Solano, J.; Rodríguez-Hernández, P.; Radescu, S.; Mujica, A.; 1089 Muñoz, A. Lattice Dynamics Study of Scheelite Tungstates under 1090 High Pressure II. PbWO₄. *Phys. Rev. B Condens. Matter Mater. Phys.* 1091 **2006**, 74 (14), 1–18.
- 1092 (91) Kaur, H.; Sinha, M. M. Lattice Dynamical Investigations of 1093 Raman and Infrared Wavenumbers of Scheelite Structured Silicates. 1094 *Phys. B Condens. Matter* **2015**, 478, 47–51.
- 1095 (92) Smirnov, M. B.; Sukhomlinov, S. V.; Smirnov, K. S. Vibrational 1096 Spectrum of Reidite ZrSiO₄ from First Principles. *Phys. Rev. B* 1097 *Condens. Matter Mater. Phys.* **2010**, 82 (9), 1–9.
- 1098 (93) Gucsik, A. Micro-Raman Spectroscopy of Reidite as an Impact-1099 Induced High Pressure Polymorph of Zircon: Experimental 1100 Investigation and Attempt to Application. *Acta Mineral.* **2006**, *47*, 1101 17–24.
- 1102 (94) Christofilos, D.; Papagelis, K.; Ves, S.; Kourouklis, G. A.; 1103 Raptis, C. High-Pressure Raman Study and Lattice Dynamical 1104 Calculations for SrWO₄. *J. Phys.: Condens. Matter* **2002**, *14* (47), 1105 12641–12650.
- 1106 (95) Christofilos, D.; Ves, S.; Kourouklis, G. A. Pressure Induced 1107 Phase Transitions in Alkaline Earth Tungstates. *Phys. Status Solidi B* 1108 **1996**, *198*, 539–544.
- 1109 (96) Khanna, R. K.; Lippincott, E. R. Infrare Spectra of Some 1110 Scheelite Structures. *Spectrochim. Acta* **1968**, *24*, 905–908.

- (97) Birch, F. Finite Strain Isotherm and Velocities for Single- 1111 Crystal and Polycrystalline NaCl at High Pressures and 300 K. J. 1112 Geophys. Res. 1978, 83, 1257.
- (98) Gonzalez-Platas, J.; Alvaro, M.; Nestola, F.; Angel, R. EosFit7- 1114 GUI: A New Graphical User Interface for Equation of State 1115 Calculations, Analyses and Teaching. *J. Appl. Crystallogr.* **2016**, 49 1116 (4), 1377–1382.
- (99) Ehlers, A. M.; Zaffiro, G.; Angel, R. J.; Boffa-Ballaran, T.; 1118 Carpenter, M. A.; Alvaro, M.; Ross, N. L. Thermoelastic Properties of 1119 Zircon: Implications for Geothermobarometry. *Am. Mineral.* **2022**, 1120 107 (1), 74–81.
- (100) Angel, R. J. Equations of State. Rev. Mineral. Geochemistry 1122 **2000**, 41 (1), 35–59.
- (101) Van Westrenen, W.; Frank, M. R.; Hanchar, J. M.; Fei, Y.; 1124 Finch, R. J.; Zha, C.-S. In Situ Determination of the Compressibility 1125 of Synthetic Pure Zircon (ZrSiO₄) and the Onset of the Zircon-1126 Reidite Phase Transformation. *Am. Mineral.* **2004**, *89*, 197–203.
- (102) Speer, J. A. The Actinide Orthosilicates. *Rev. Mineral.* 1128 *Geochem.* 1982, 5, 113–136.
- (103) Marcial, J.; Zhang, Y.; Zhao, X.; Xu, H.; Mesbah, A.; Nienhuis, 1130 E. T.; Szenknect, S.; Neuefeind, J. C.; Lin, J.; Qi, L.; et al. 1131 Thermodynamic Non-Ideality and Disorder Heterogeneity in 1132 Actinide Silicate Solid Solutions. *npj Mater. Degrad.* **2021**, *5*, 34.
- (104) Li, H.; Zhou, S.; Zhang, S. The Relationship between the 1134 Thermal Expansions and Structures of ABO₄ Oxides. *J. Solid State* 1135 *Chem.* **200**7, 180 (2), 589–595.
- (105) Scott, H. P.; Williams, Q.; Knittle, E. Ultralow Compressibility 1137 Silicate without Highly Coordinated Silicon. *Phys. Rev. Lett.* **2001**, 88 1138 (1), 015506.
- (106) Hazen, R. M.; Finger, L. W.; Mariathasan, J. W. E. High- 1140 Pressure Crystal Chemistry of Scheelite-Type Tungstates and 1141 Molybdates. J. Phys. Chem. Solids 1985, 46 (2), 253–263.
- (107) Anderson, D. L.; Anderson, O. L. The Bulk Modulus-Volume 1143 Relationship for Oxides. *J. Geophys. Res.* **1970**, *75* (17), 3494–3500. 1144
- (108) Xu, H.; Zhao, Y.; Zhang, J.; Wang, Y.; Hickmott, D. D.; 1145 Daemen, L. L.; Hartl, M. A.; Wang, L. Anisotropic Elasticity of 1146 Jarosite: A High-P Synchrotron XRD Study. *Am. Mineral.* **2010**, 95 1147 (1), 19–23.
- (109) Hazen, R. M.; Finger, L. W. Bulk Modulus-Volume Rationship 1149 for Cation-Anion Polyhedra. *J. Geophys. Res.* **1979**, 84 (12), 6723–1150 6728.
- (110) Anderson, O. L.; Nafe, J. E. The Bulk Modulus-Volume 1152 Rationship for Oxide Compounds and Related Geophysical Problems. 1153 *J. Geophys. Res.* **1965**, 70 (16), 3951–3962.
- (111) Hazen, R. M.; Downs, R. T.; Prewitt, C. T. Principles of 1155 Comparative Crystal Chemistry. *Rev. Mineral. Geochemistry* **2000**, 41 1156 (1), 1–33.
- (112) Crocombette, J. P.; Ghaleb, D. Modeling the Structure of 1158 Zircon (ZrSiO₄): Empirical Potentials, Ab Initio Electronic Structure. 1159 *J. Nucl. Mater.* **1998**, 257 (3), 282–286.
- (113) Mondal, S. K.; Das, P. K.; Mandal, N.; Arya, A. A Novel 1161 Approach to the Structural Distortions of U/Th Snub-Disphenoids 1162 and Their Control on Zircon \rightarrow Reidite Type Phase Transitions of 1163 $U_{1-X}Th_xSiO_4$. J. Phys.: Condens. Matter 2020, 32 (14), 145401.
- (114) Chaplot, S. L.; Pintschovius, L.; Choudhury, N.; Mittal, R. 1165 Phonon Dispersion Relations, Phase Transitions, and Thermody- 1166 namic Properties of ZrSiO₄: Inelastic Neutron Scattering Experi- 1167 ments, Shell Model, and First-Principles Calculations. *Phys. Rev. B* 1168 *Condens. Matter Mater. Phys.* **2006**, 73 (9), 1–8.
- (115) Mouri, T.; Enami, M. Raman Spectroscopic Study of Olivine- 1170 Group Minerals. *J. Mineral. Petrol. Sci.* **2008**, *103* (2), 100–104. 1171
- (116) Williams, Q.; Knittle, E.; Reichlin, R.; Martin, S.; Jeanloz, R. 1172 Structural and Electronic Properties of Fe₂SiO₄-Fayalite at Ultrahigh 1173 Pressures: Amorphization and Gap Closure. *J. Geophys. Res.* **1990**, 95 1174 (B13), 21549–21563.
- (117) Liu, L. G.; Mernagh, T. P. Raman Spectra of Forsterite and 1176 Fayalite at High Pressures and Room Temperature. *High Press. Res.* 1177 **1993**, 11 (5), 241–256.

- 1179 (118) Mernagh, T. P.; Liu, L.-G. Pressure Dependence of Raman 1180 Spectra from the Garnet End-Members Pyrope, Grossularite, and 1181 Almandite. *J. Raman Spectrosc.* **1990**, *21*, 305–309.
- 1182 (119) Mulligan, S. Ř.; Stavrou, E.; Chariton, S.; Tschauner, O.; 1183 Salamat, A.; Wells, M. L.; Smith, A. G.; Hoisch, T. D.; Prakapenka, V.
- 1184 Equation of State for Natural Almandine, Spessartine, Pyrope Garnet:
- 1185 Implications for Quartz-in-Garnet Elastic Geobarometry. *Minerals* 1186 **2021**, *11* (5), 458.
- 1187 (120) Mernagh, T. P.; Liu, L.-G. Raman Spectra from the $\rm Al_2SiO_5$
- 1188 Polymorphs at High Pressures and Room Temperature. Phys. Chem.
- 1189 Miner. **1991**, 18 (2), 126-130.